

Dong, Yulian; Yan, Chengzhan; Zhao, Huaping; Lei, Yong

Recent advances in 2D heterostructures as advanced electrode materials for potassium-ion batteries

Original published in: Small structures. - Weinheim : Wiley-VCH. - 3 (2022), 3, art. 2100221, 19 pp.
Original published: 2022-01-22
ISSN: 2688-4062
DOI: [10.1002/sstr.202100221](https://doi.org/10.1002/sstr.202100221)
[Visited: 2022-05-16]



This work is licensed under a [Creative Commons Attribution 4.0 International license](https://creativecommons.org/licenses/by/4.0/). To view a copy of this license, visit <https://creativecommons.org/licenses/by/4.0/>

Recent Advances in 2D Heterostructures as Advanced Electrode Materials for Potassium-Ion Batteries

Yulian Dong, Chengzhan Yan, Huaping Zhao, and Yong Lei*

Owing to the cost-effectiveness, Earth abundance, and suitable redox potential, potassium-ion batteries (PIBs) stand out as one of the best candidates for large-scale energy storage systems. However, the large radius of K^+ and the unsatisfied specific capacity are the main challenges for their commercial applications. To address these challenges, constructing heterostructures by selecting and integrating 2D materials as host and other materials as guest are proposed as an emerging strategy to obtain electrode materials with high capacity and long life-span, thus improving the energy storage capability of PIBs. Recently, numerous studies are devoted to developing 2D-based heterostructures as electrode materials for PIBs, and significant progress is achieved. However, there is a lack of a review article for systematically summarizing the recent advances and profoundly understanding the relationship between heterostructure electrodes and their performance. In this sense, it is essential to outline the promising advanced features, to summarize the electrochemical properties and performances, and to discuss future research focuses about 2D-based heterostructures in PIBs.

(-2.93 V vs. standard hydrogen electrode [SHE] for K^+/K is close to -3.04 V vs. SHE for Li^+/Li) enables a similar operating voltage to LIBs, thus assuring a high energy density.^[9,10] Third, attributed to the small Stokes radius of solvated K^+ , it will facilitate the rapid shuttle of K^+ in electrolytes.^[11–13] However, the performance of PIBs is severely restricted by the large radius of K^+ .^[14,15] The large radius of K^+ exhibit a poor ion diffusivity in solid-state electrodes, resulting in slow K^+ reaction kinetics and unsatisfactory rate performance of PIBs. Meanwhile, the insertion/extraction of large K^+ causes large volume variations and thereafter pulverization of electrode materials, leading to the low cycling stability of PIBs.^[16,17] To this end, it is critical to use host materials that have the superior capability to reversibly store amounts of K^+ and sufficient structural stability to withstand the repeated potassiation/depotassiation processes.


1. Introduction

Renewable and sustainable energy sources, like solar, wind, geothermal, hydropower, wave, and tidal power, are essential to address the ever-increasing challenges in energy consumption and environmental deterioration.^[1] At the same time, the optimal use of electricity generated from these intermittent energy resources requires the development of large-scale and low-cost stationary energy storage systems.^[2–4] Currently, considerable efforts are devoted to developing stationary energy storage systems based on potassium-ion batteries (PIBs), owing to the specific advantages of PIBs compared with lithium-ion batteries (LIBs) (Figure 1a).^[5–7] First of all, the high abundance and low cost of potassium resources make PIBs more cost-effective than LIBs.^[8] Second, a suitable reduction potential of potassium

efficient structural stability to withstand the repeated potassiation/depotassiation processes.

Among candidates of host materials for K^+ insertion,^[18] 2D materials have drawn remarkable interests, and they mainly include elemental 2D materials (such as graphene and phosphorene),^[19,20] transition metal carbides/nitrides (MXenes, such as Ti_2C and Ti_3CN),^[21,22] transition metal dichalcogenides (TMDs, such as MoS_2 , $MoSe_2$, and WS_2),^[23–26] and transition metal oxides (TMOs) with layered structures (such as V_2O_5 and MoO_3)^[27,28] (Figure 1b,c). Their unique layered structure provides short ion-diffusion channels for rapid K^+ transportation and their large surface areas offer abundant active sites for K^+ adsorption.^[29,30] Moreover, the interlayer weak van der Waals (vdW) forces endow 2D materials with good mechanical flexibility, which can accommodate large K^+ without deteriorating the structural integrity of the electrode during the K insertion/extraction processes.^[30] However, till now, none of these 2D materials yet have exhibited fully satisfactory capabilities for K^+ storage. For example, the surface-dependent charge storage mechanism restricts the limited capacity of graphene-based materials.^[31] For TMDs, a changeable charge storage mechanism from intercalation to conversion reaction undergoing the first discharge cycle leads to poor capacity retention of TMDs.^[32,33] With respect to TMOs, the rate performance is mainly limited by the poor electronic conductivity of TMOs.^[34–36] For MXenes, the reversible capacity varies with the alternation of surface functional groups inherently incorporated during the MXenes synthesis process.^[37,38] So far, various strategies have been proposed to solve these aforementioned

Y. Dong, C. Yan, H. Zhao, Y. Lei
Fachgebiet Angewandte Nanophysik
Institut für Physik & IMN MacroNano
Technische Universität Ilmenau
98693 Ilmenau, Germany
E-mail: yong.lei@tu-ilmenau.de

 The ORCID identification number(s) for the author(s) of this article can be found under <https://doi.org/10.1002/sstr.202100221>.

© 2022 The Authors. Small Structures published by Wiley-VCH GmbH. This is an open access article under the terms of the Creative Commons Attribution License, which permits use, distribution and reproduction in any medium, provided the original work is properly cited.

DOI: 10.1002/sstr.202100221

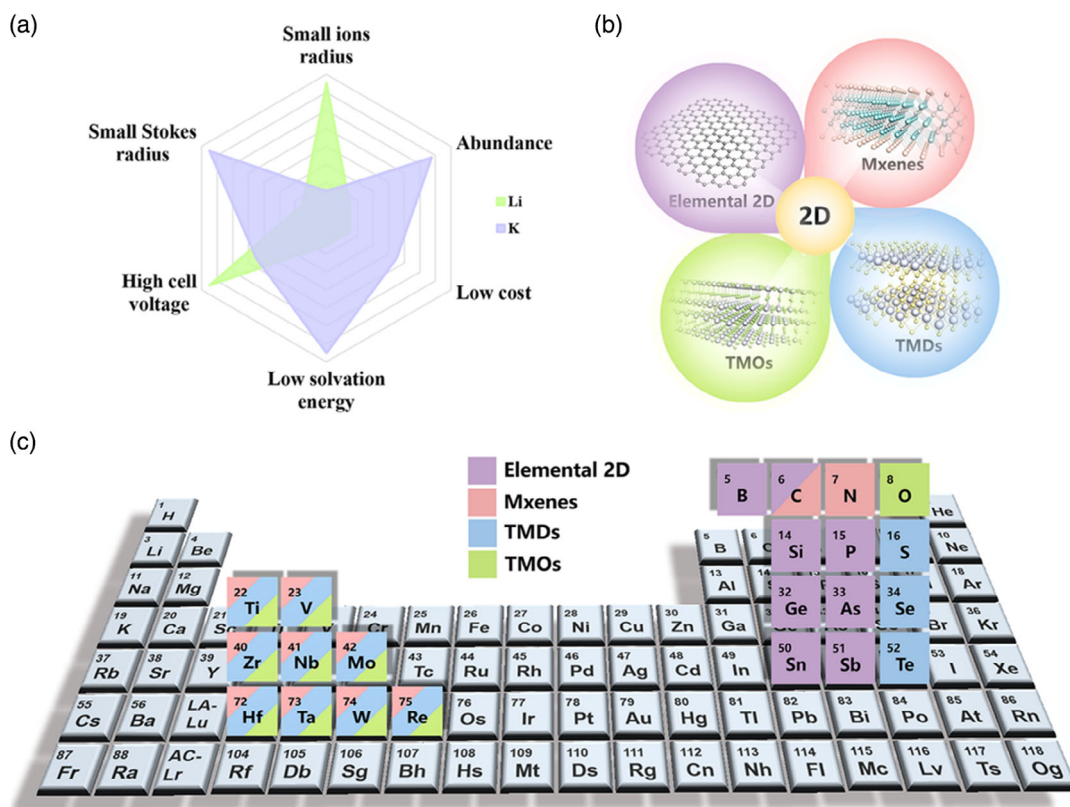


Figure 1. a) The comparison of crucial parameters between LIBs and PIBs. b) Schematic of the representative structure of 2D atomic crystals. c) Typical 2D materials.

issues, and the representative ones include expanding layer spacing,^[39,40] creating structural defects,^[41–44] fabricating porous structures,^[45,46] constructing heterostructures,^[47,48] and surface/interface engineering.^[49,50] In particular, constructing heterostructures based on different 2D materials as host and other materials as guest (depicted as 2D-based heterostructures) is a highly effective strategy because 2D-based heterostructures can offer the opportunity to combine the advantages of 2D materials and meanwhile eliminate the disadvantages of individual counterparts.^[51,52] Up to now, many 2D-based heterostructures with different compositions and morphologies have been designed, fabricated, and investigated as electrode materials for improving the energy storage performance of PIBs.

Given the rapid progress in the past few years, a timely summary in the field of 2D-based heterostructures for PIB application has to be conducted. Herein, we provide a comprehensive review of recent advances in developing 2D-based heterostructures as electrode materials for PIBs. We first summarize the advanced properties of 2D-based heterostructures for PIB applications. By highlighting some typical examples (mainly including graphene-based, MXenes-based, TMD/TMOs-based heterostructures), we then introduce the main characteristics of 2D-based heterostructures for K^+ storage and emphasize their synergic effects on optimizing electrochemical performance. Finally, we also provide an outlook on challenges and perspectives associated with 2D-based heterostructures for future PIB applications.

2. Advanced Features of 2D-Based Heterostructures for PIBs

Owing to the unique physicochemical properties, 2D-based heterostructures have been widely investigated as building blocks for future (opto-)electronics and as advanced catalysts for (photo-)electrocatalysis.^[53–55] Likewise, constructing 2D-based heterostructures is also revealed to provide unprecedented potentials for boosting the electrochemical performance (i.e., capacity, rate capability, and stability) of 2D materials as electrode materials for PIBs.^[56–58] As shown in **Figure 2**, many 2D materials have been assembled with other materials (e.g., 0D, 1D, 2D, or 3D) via either weak interstratification (vdW force or electrostatic attraction) or covalent bond to form 2D-based heterostructures.^[48,59–61] When integrating host 2D materials with guest functional materials, the as-obtained 2D-based heterostructures will possess enlarged interface contact and increased interlayer distance. The enlarged interface contact offers more electrochemical active sites for K^+ storage, while the increased interlayer distance in heterostructures ensures rapid diffusion of K^+ and compensates structural changes during the K^+ insertion/extraction process.^[61–63] Moreover, due to the lattice constant differences between host 2D materials and guest functional materials, vacancies and/or distortions will be generated at the heterointerfaces in 2D-based heterostructures, which will provide additional active sites for K^+ storage.^[64] Besides the difference

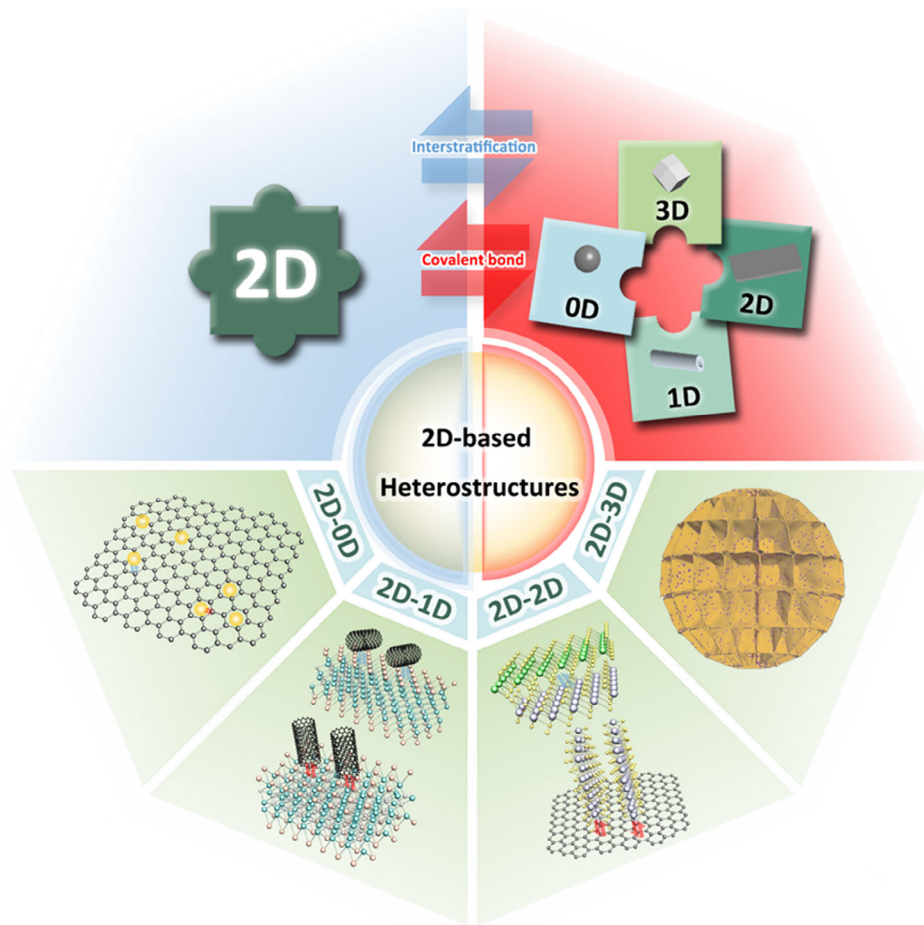


Figure 2. Scheme of different kinds of 2D-based heterostructures constructed by assembling host 2D materials with guest 0D, 1D, 2D, or 3D materials for the enhanced PIB performance.

in the lattice constant, host 2D materials and guest functional materials generally have different energy bandgaps.^[65] Both theoretical and experimental studies suggest that the difference in their energy bandgaps will generate a built-in electric field in heterostructures. This additional electric field can facilitate the rapid transportation of electrons in the electrodes during the K^+ insertion/extraction process, which enhances the charge transfer kinetics. Moreover, the existence of a built-in electric field in the heterostructures will also result in the redistribution of charges at the heterointerfaces, which further improves the conductivity of the heterostructures.^[66] In addition, constructing heterostructures is also an effective way to avoid restacking and agglomeration of 2D materials during the charging and discharging process.^[67,68] Attributed to these advanced features mentioned earlier, various 2D-based heterostructures consisting of different compositions and with different morphologies have been designed, synthesized, and studied as electrode materials for PIBs (Figure 2). By optimizing the compositions and morphologies of 2D-based heterostructures, it will offer the opportunity to further maximize the K^+ storage of 2D-based heterostructures.

3. Electrochemical Performance of 2D-Based Heterostructures for PIBs

3.1. Graphene-Based Heterostructures

As known, there are many forms of carbon materials, such as graphite, graphene, hard carbon, and soft carbon materials.^[69–72] Among them, graphite with a theoretical specific capacity of 279 mAh g^{-1} (corresponding to the formation of KC_8) and a low working voltage ($<0.4 \text{ V vs. } K/K^+$) has attracted considerable interest as PIB anode materials.^[73,74] So far, some strategies have been developed to further improve the capacity of graphite for PIBs. For example, bulk graphite has been exfoliated into monolayer or a few layers of graphene to provide more active sites on the sides of the graphene layer or functionalized graphene layer and finally delivers a high specific capacity over 350 mAh g^{-1} .^[75] However, the aggregation of graphene with monolayer or a few layers will lead to the reduction of active sites for K^+ absorption. To this end, constructing graphene-based heterostructures is proposed to enhance K^+ storage performance. This strategy could effectively prevent the stacking of graphene and enable to enhance the capacity by

combining with high theoretical specific capacity materials, such as Sb (660 mAh g⁻¹) and SnS₂ (733 mAh g⁻¹),^[62,76–78]

As is known, the small size of nanodots and nanoparticles can reduce the ion diffusion length; thus, Wu and co-workers proposed the fabrication of 2D–0D heterostructures to shorten the ion diffusion length and improve the electrochemical performance.^[62] They constructed heterostructures consisting of SnSb₂Te₄ nanodots and few-layer graphene (SnSb₂Te₄/G) via a ball-milling method (Figure 3a). The SnSb₂Te₄ with good conductivity and large interlayer spacing can guarantee high specific capacity and provide open ion-diffusion channels (Figure 3b).^[62] It was worth noting that SnSb₂Te₄ is a new quantum material with unique structure, where electrons can only move freely along the 2D surface of the material. Therefore, increasing the surface area of SnSb₂Te₄ can improve its conductivity by expanding lateral space. As an anode in PIBs, the SnSb₂Te₄/G heterostructures not only exhibited an excellent discharge specific capacity of 450, 362, 325, 289, 255, 215, and 153 mAh g⁻¹ at different current densities of 0.05, 0.1, 0.2, 0.5, 1, 2, 5 A g⁻¹, respectively (Figure 3c),^[62] but also improved the surface pseudocapacitance as high as 66.3% in the whole capacity charge storage at a scan rate of 0.8 mV s⁻¹. The good electrochemical performance was attributed to accelerating the transportation of ions/electrons by the p–n heterojunction (Figure 3d,e). In addition, forming heterostructures also resulted in strong electronic coupling between SnSb₂Te₄ and Te-doped graphene to ensure structural and cycling stability. In another example, phosphorus nanoparticles were uniformly embedded in reduced graphene oxide (P@RGO heterostructures) via vaporization heating treatment in a stainless-steel autoclave (Figure 3f).^[79] The presence of strong P–C covalent bonds could adhere P nanoparticles in the RGO host and obtain the active materials with enlarged interlayer spacing (Figure 3g), which is beneficial for the structural durability of the electrode materials during the cycling process. As a result, the P@RGO heterostructures presented a high discharge/charge capacity of 628.7 and 521.4 mAh g⁻¹ in the second cycle, at 100 mA g⁻¹. Even at 500 mA g⁻¹, it also could keep a capacity of 253 mAh g⁻¹ after 500 cycles (Figure 3h). Vishnuprakash et al. fabricated V₂O₅ nanorod@rGO heterostructures, in which V₂O₅ nanorods were supported by rGO nanosheets to offer more active sites.^[80] The V₂O₅ nanorod@rGO heterostructures showed a good specific capacity and a long cycle life as a cathode electrode for PIBs. After 500 cycles, the capacity was retained as high as 271 mAh g⁻¹ (about 80% of its initial discharge capacity). It still delivered the capacity of 50 mAh g⁻¹ at the high current density of 2940 mA g⁻¹.

Compared with individual 2D materials, the 2D–2D heterostructures offer a novel platform to improve the K⁺ storage performance. The 2D–2D vdW heterostructures of BiSbOCl/rGO were synthesized as electrode materials for PIBs.^[61] As shown in Figure 4a,b, bimetallic oxychloride nanosheets with Bi and Sb dispersed on rGO nanosheets via vdW force. The 2D vdW heterostructures in the form of nanosheets/nanosheets (NS/NS) displayed the strongest vdW force than that of nanoparticles/nanoparticles (NP/NP) and nanoparticles/nanosheets (NP/NS), which enlarged the contact area between the nanosheets (Figure 4c). Thus, the Bi_{0.51}Sb_{0.49}OCl/rGO heterostructures showed ultralong stability (running 9 months) with a

Coulombic efficiency (CE) close to 100% even after 1000 cycles, at 100 mA g⁻¹ (Figure 4d), and delivered a high discharge capacity of 407 mAh g⁻¹ at 100 mA g⁻¹. To explore the practicability, full-cell PIBs were assembled with Bi_{0.51}Sb_{0.49}OCl/rGO heterostructures as anode and perylenetetracarboxylic dianhydride (PTCDA) as cathode. The full cell presented a high discharge capacity of 225 mAh g⁻¹ after 50 cycles (Figure 4e). They also investigated the K⁺ storage mechanism by operando X-ray diffraction (XRD). During discharging in the first cycle, the lattice of Bi_{0.51}Sb_{0.49}OCl underwent irreversible changes because Bi³⁺ and Sb³⁺ were reduced to Bi and Sb, respectively. Then, the further alloying reaction between Bi–Sb alloy and K⁺ was carried out to deliver the additional specific capacity. In addition, the experiments demonstrated that the ratio of Bi, Cl, and Sb in the precursors was vital to synthesizing the uniform 2D vdW heterostructures of Bi_{0.51}Sb_{0.49}OCl nanosheets on the rGO nanosheets.^[61] In another case, the 2D–2D multilayered heterostructures of VOPO₄–graphene was fabricated as a zero-strain cathode material for PIBs (Figure 4f).^[81] By adjusting the mass ratio between VOPO₄ nanosheets and cationic-surfactant-modified graphene, self-assembled VOPO₄–graphene multilayered heterostructures were obtained. The lattice strain of VOPO₄–graphene heterostructures was confirmed to be 3.2% through Raman spectroscopy mapping and density functional theory (DFT) calculations. The lower strain of the crystalline lattices in VOPO₄–graphene heterostructures benefited from the intercalation/deintercalation of larger K⁺ compared with simply restacked VOPO₄ nanoflakes. The in situ XRD characterizations revealed that there was only a 2.0% volume change for VOPO₄–graphene multilayered heterostructures during cycling. These results demonstrated the superiority of heterostructures. After 100 cycles, the stable reversible capacity was as high as 160 mAh g⁻¹ at 16 mA g⁻¹ without obvious capacity decay. Even under a high current density of 3200 mA g⁻¹, it still maintained 80 mAh g⁻¹. The good electrochemical performance is attributed to the robust 2D multilayered heterostructures.^[81]

In addition to the aforementioned 2D heterostructures via layer-by-layer assembly, the 2D materials also can be vertically grown on another type of 2D material to form a novel kind of 2D heterostructure. For example, Xie et al. reported the heterostructures of ultrathin MoS₂ vertically grown on rGO through a two-step solvothermal method (Figure 5a).^[63] These MoS₂/rGO heterostructures were tightly coupled by C–O–Mo bonds between MoS₂ and rGO. The unique heterostructures not only expanded the MoS₂ layer spacing from 0.63 to 0.93 nm but also restrained the self-stacking of 2D and increased the active area (Figure 5b). It provided the pathway for rapid ionic and electronic transportation, which enabled to deliver a high rate capacity (Figure 5c). This vertical heterostructures could increase the contact area between the active material and the electrolyte, resulting in a charming pseudocapacitance. On the contrary, some research suggests that such kinds of heterostructures are easily destroyed and agglomerated after certain cycles due to the shuttle effect of polysulfides. For example, layer-by-layer 2D vdW heterostructures (C/MoS₂/G) and self-assembled vertical covalent bond heterostructures (MoS₂/G) were designed and fabricated.^[82] The C/MoS₂/G vdW heterostructures were prepared by combining oxidative polymerization and postsulfidation. In brief, the heterostructure precursors were first anchored on

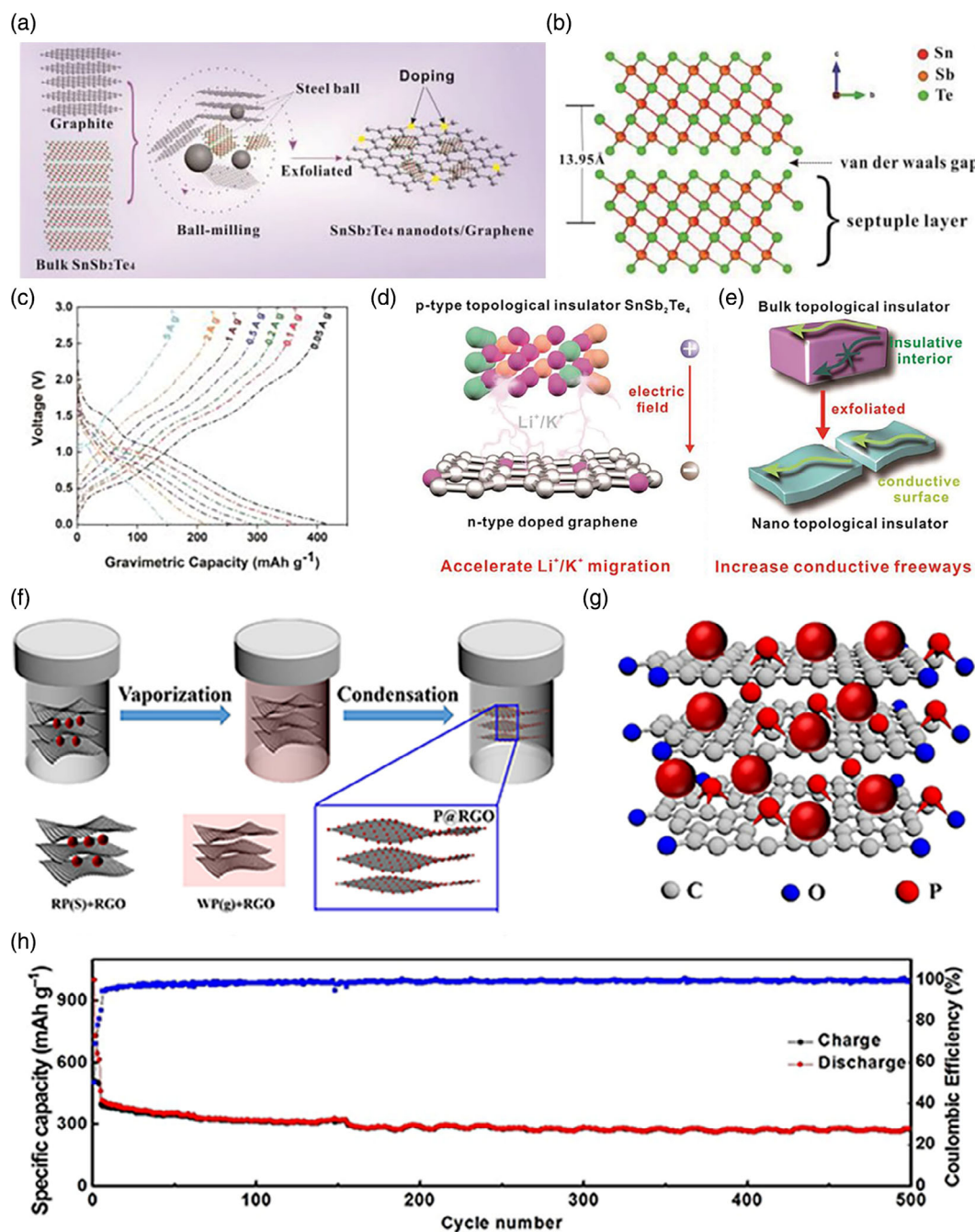


Figure 3. a) Schematic illustration of preparing SnSb₂Te₄/G heterostructures. b) Crystal structure of SnSb₂Te₄. c) Galvanostatic charge–discharge curves of SnSb₂Te₄/G at different current densities. d) Schematic diagram of the relationship between the electric field and the Li⁺/K⁺ transport kinetics in SnSb₂Te₄/G heterostructures. e) Increased conductive freeways of SnSb₂Te₄. a–e) Reproduced with permission.^[62] Copyright 2019, Wiley-VCH. f) Schematic of the P@RGO preparation process. g) Illustration of RP nanoparticles embedded in RGO. h) The long cycling stability of P@RGO at 500 mA g⁻¹. f–h) Reproduced with permission.^[79] Copyright 2018, Wiley-VCH.

GO by introducing the induced reagent and then thermal sulfidation in a reduction environment was conducted. In comparison with MoS₂/G that MoS₂ nanosheets were vertically grown on graphene (Figure 5d), MoS₂ nanosheets in the C/MoS₂/G vdW heterostructures were confined by graphene and amorphous carbon, which could effectively prevent the agglomeration of the

MoS₂ nanosheets and offer space to buffer huge volume changes of MoS₂ and release the mechanical stress during cycling. In addition, the C/MoS₂/G heterostructures also inhibited the dissolution of intermediate polysulfide products into the electrolyte to realize an ultralong lifespan of 4000 cycles at a high current density of 5 A g⁻¹ (Figure 5e).^[82]

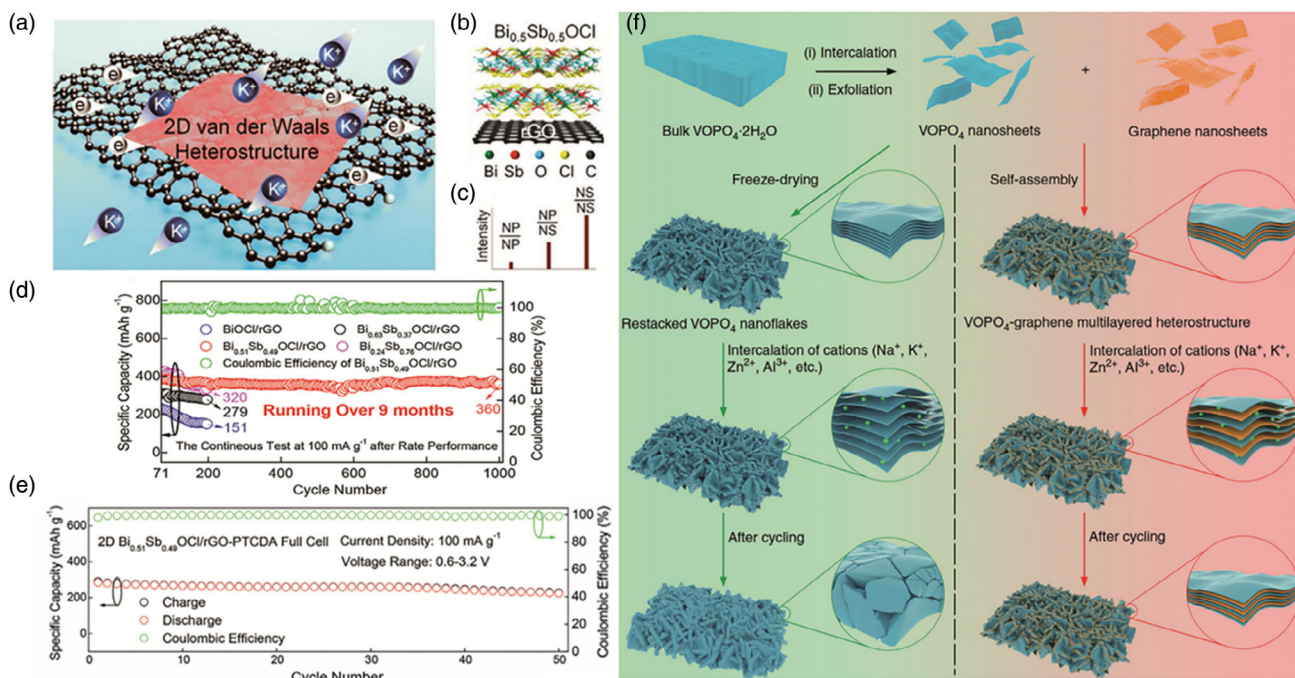


Figure 4. Illustration of a) top view and b) cross-section view of $\text{Bi}_{0.51}\text{Sb}_{0.49}\text{OCl}/\text{rGO}$. c) Demonstration of the relative intensity of vdW force between various assembling of nanoparticle and nanosheets. d) The cycling performance of BiOCl/rGO , $\text{Bi}_{0.63}\text{Sb}_{0.37}\text{OCl}/\text{rGO}$, $\text{Bi}_{0.51}\text{Sb}_{0.49}\text{OCl}/\text{rGO}$, and $\text{Bi}_{0.24}\text{Sb}_{0.76}\text{OCl}/\text{rGO}$ at 100 mA g^{-1} . e) Cycling performance of the PIB full cell under 100 mA g^{-1} from 0.6 to 3.2 V. a–e) Reproduced with permission.^[61] Copyright 2020, Wiley-VCH. f) Illustration of preparing 2D multilayered heterostructures by self-assembly between VOPO_4 nanosheets and graphene. f) Reproduced with permission.^[81] Copyright 2020, Springer Nature.

The 3D–2D $\text{Bi}_2\text{S}_3@\text{rGO}$ heterostructures under the assistance of the visible light irradiation were constructed.^[83] Owing to the different Fermi levels between rGO and Bi_2S_3 microspheres, a built-in electric field was introduced at the Bi_2S_3 -rGO heterointerface with the electric field direction from rGO to Bi_2S_3 . This built-in electric field in 3D–2D $\text{Bi}_2\text{S}_3@\text{rGO}$ heterostructures was proved to facilitate the K^+ transport.^[83] As a result, $\text{Bi}_2\text{S}_3@\text{rGO}$ exhibited a remarkable rate capability (237 mAh g^{-1} at 2 A g^{-1} after 300 cycles) and delivered a high specific capacity of 538 mAh g^{-1} at 0.2 A g^{-1} . In another example, bimetallic selenides ($\text{MoSe}_2/\text{CoSe}_2$) were wrapped in N-, S-co-doped porous hollow carbon nanospheres with rGO ($\text{rGO}@\text{MCSe}$).^[84] When $\text{rGO}@\text{MCSe}$ was served as an anode for PIBs, it displayed a high reversible capacity of 417.8 mAh g^{-1} at 0.1 A g^{-1} after 100 cycles and a high rate capability performance of 310.4 mAh g^{-1} at 5 A g^{-1} .

In summary, graphene and/or functional graphene can support the mixed-dimensional materials by either vdW forces or covalent bonds. Generally, graphene layers not only work as the highly conductive matrix but also alleviate the volume expansion. Meanwhile, the construction of graphene-based heterostructures can impede the self-stacking of graphene nanosheets and increase the absorbing active sites. Therefore, both the potassium storage capacity and the lifespan of graphene-based heterostructures can be promoted.

3.2. MXenes-Based Heterostructures

MXenes ($\text{Ti}_3\text{C}_2\text{T}_x$, in which T_x represents surficial termination groups such as $-\text{OH}$, $-\text{F}$, etc.) are novel kinds of 2D

materials.^[85–87] Due to their outstanding electrical conductivity, ionic conductivity, scalable layer spacing, and open 2D channel, MXenes have been widely applied in the fields of energy storage,^[88,89] catalysis,^[90] supercapacitors,^[91,92] and so on. In 2013, the electrochemical behavior of MXenes in PIBs was first investigated.^[93] The DFT results demonstrate that K atoms can be adsorbed on the surface of Ti_3C_2 and the capacity of Ti_3C_2 can reach 191.8 mAh g^{-1} . Further researches have identified that the composition, surface chemistry, and structural construction of MXenes have significant effect on their electrochemical properties.^[21,93] A series of cations (like Li^+ , K^+ , and Al^{3+}) can be intercalated into $\text{Ti}_3\text{C}_2\text{T}_x$ nanosheets, which reveals the great potentials of MXenes as electrode materials for batteries.^[36,94] For example, $\text{K}_2\text{Ti}_4\text{O}_9$ nanoribbons showed a reversible capacity of 151 mAh g^{-1} at 50 mA g^{-1} when being applied as electrode materials for PIBs.^[21] Although MXenes provide a rich chemically active interface and short ion-diffusion length, their specific capacity is still not satisfied. Therefore, advanced MXenes need to be further developed to achieve better electrochemical performance.^[93–96]

As known, quantum dots with ultrasmall size would shorten the K^+ diffusion path, but the high surface energy of quantum dots easily leads to the agglomeration of quantum dots. To this end, Cao et al. designed and synthesized 0D–2D heterostructures composed of $\text{Cu}_{12}\text{Sb}_4\text{S}_{13}$ quantum dots and few-layer Ti_3C_2 (named CAS– Ti_3C_2) via a multistep process (Figure 6a) and investigated as an anode for PIBs.^[97] $\text{Cu}_{12}\text{Sb}_4\text{S}_{13}$ quantum dots were easily anchored onto the host Ti_3C_2 nanosheets under

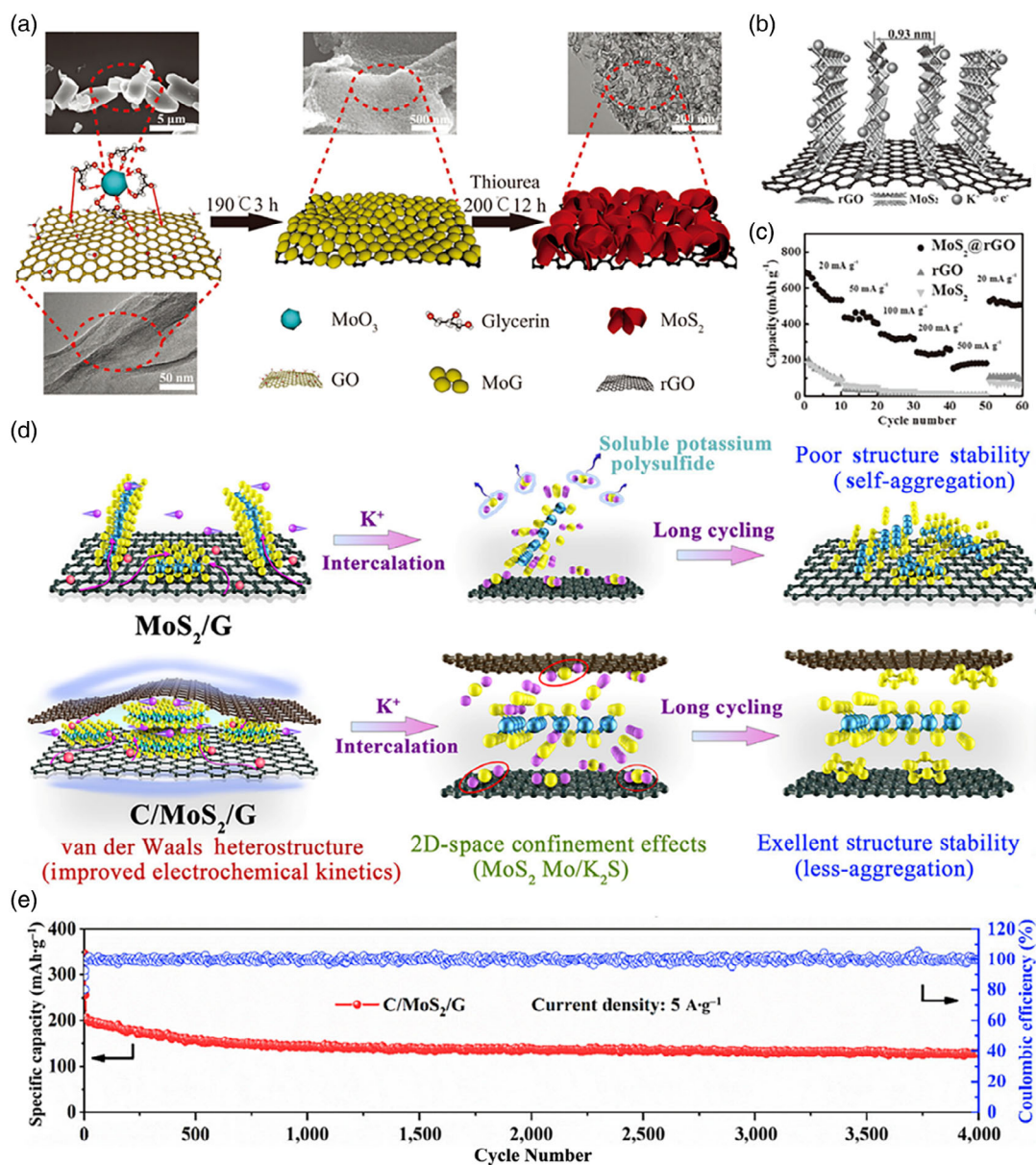


Figure 5. a) Illustrating the fabrication process of MoS₂ vertically grown on rGO sheets. b) Schematic diagram of pathways in the MoS₂@rGO heterostructures for K⁺ diffusion and electron conduction. c) Rate performance of MoS₂@rGO, MoS₂ particle, and pure rGO anodes from 20 to 500 mA g⁻¹. a–c) Reproduced with permission.^[63] Copyright 2017, Wiley-VCH. d) Schematic illustration of the structural evolution of C/MoS₂/G and MoS₂/G heterostructures during long-term cycling. e) The cycling performance of C/MoS₂/G heterostructures at a current density of 5 A g⁻¹. d,e) Reproduced with permission.^[82] Copyright 2021, Springer Nature.

sonication. Due to the presence of the strong Ti–S bonds between Cu₁₂Sb₄S₁₃ quantum dots and Ti₃C₂ nanosheets, the CAS–Ti₃C₂ heterostructures can not only restrain the agglomeration of active materials but also ensure the good structural stability of heterostructures. In addition, CAS–Ti₃C₂ heterostructures exhibited an insertion–conversion–alloying mechanism for K⁺ storage. The CAS–Ti₃C₂ heterostructures delivered an ultrahigh initial specific capacity of 1582.7/905.6 mAh g⁻¹ (discharge/charge) at 50 mA g⁻¹, corresponding CE of 57.2% (Figure 6b). The CAS–Ti₃C₂ exhibited a high CE of

≈100% in the following cycles, which implied the high reversible capacity. It also displayed an ultralong cycling life up to 1800 cycles at 1.0 A g⁻¹ with a capacity of 175.6 mAh g⁻¹ (Figure 6c).

Furthermore, 2D–1D heterostructures of MXene@N-doped carbonaceous nanofibers were fabricated as PIB anode, which presented a reversible capacity (349.2 mAh g⁻¹ at 0.1 A g⁻¹) and an ultralong lifespan (201.5 mAh g⁻¹ at 1 A g⁻¹ after 1800 cycles).^[98] The ultrastable electrochemical performance was attributed to the high-density distribution of 2D MXenes on N-doped carbon nanofiber and the formation of self-supported

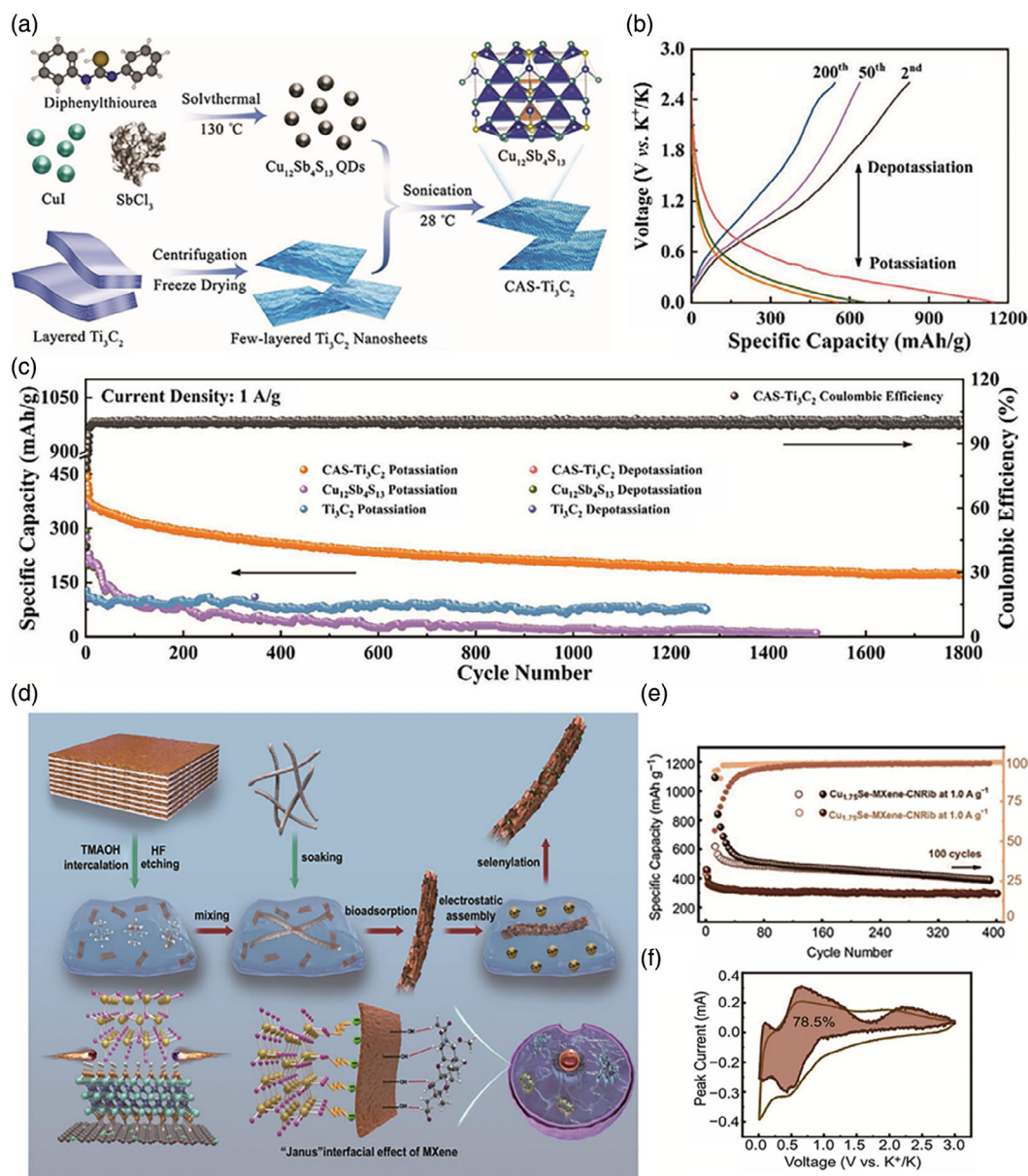


Figure 6. a) Scheme for the fabrication of CAS–Ti₃C₂ heterostructures. b) Charge–discharge profiles of CAS–Ti₃C₂ heterostructures between 0.01 and 2.6 V. c) Cycling performance comparison of CAS–Ti₃C₂ heterostructures, Cu₁₂Sb₄S₁₃ quantum dots, and Ti₃C₂ nanosheets. a–c) Reproduced with permission.^[97] Copyright 2021, Wiley-VCH. d) Schematic illustration of MSE on MXene-coated fungal-derived CNRib heterostructures. e) Cycling performance at 0.1 and 1.0 A g⁻¹ and f) the pseudocapacitive-dominated proportions at the sweep rates of 1.0 mV s⁻¹ of Cu_{1.75}Se–MXene–CNRib heterostructures. d–f) Reproduced with permission.^[99] Copyright 2021, Springer Nature.

porous heterostructures. The unique structure can take full advantages of the high surface-controlled capacitive storage of 2D MXenes and the rapid electron transfer of 1D N-doped carbon nanofiber. It is also found that strongly coupled 2D transition metal chalcogenide–MXene–carbonaceous nanoribbons (MSe–MXene–CNRib) have excellent Na⁺/K⁺-ion storage performance.^[99] Transition metal selenides (including Cu_{1.75}Se, NiSe₂, and CoSe₂) were anchored on one surface of the MXene nanosheets by coupling with terminated groups, while the carbonaceous nanoribbons (CNRib) were attached on

another surface of MXene nanosheets via amino bridging groups and hydrogen bonds to obtain unique heterostructures (Figure 6d). These unique MXenes-based heterostructures could present a “Janus” interfacial effect with different bonds’ interaction, which was joined via strong chemical bonds rather than vdW forces. Serving as anode electrode for PIBs, the Cu_{1.75}Se–MXene–CNRib electrode maintained a high reversible capacity of 305.6 mAh g⁻¹ at a high current density of 1.0 A g⁻¹ after 400 cycles (Figure 6e). In addition, the pseudocapacitive storage contributed a high ratio of 78.5% on the whole

capacity storage (Figure 6f).^[99] The results indicated that Cu_{1.75}Se–MXene–CNRib electrode was favorable for surface-dominated K⁺ storage, particularly at high rates. Furthermore, the DFT calculations were conducted to verify the possibility of the diffusion behaviors of K⁺ at the interface of the heterostructures. It confirmed that the MSe–MXene–CNRib electrode showed improved electronic conductivities and reduced diffusion barriers, which were supposed to boost the K⁺ adsorption and diffusion kinetics. Obviously, the unique ternary heterostructures offered plenty of active sites and additional storage interfaces, ensuring the heterostructures for excellent cycling stability and fast transport for big alkali metal ions.

To further enhance the electrochemical performance of MXenes-based materials, various 2D–2D heterostructures based on MXenes have been designed and fabricated. For example, Li et al. synthesized layered Ti₃C₂T_x MXene/MoS₂ heterostructures and they displayed a reversible capacity of 290.7 mAh g⁻¹ at 0.05 A g⁻¹ as PIB electrode materials.^[100] Recently, novel carbon-coated MoSe₂/MXene heterostructures were fabricated by a multistep reaction.^[101] As shown in Figure 7a, MoSe₂ nanosheets were vertically anchored on the MXene substrate with Ti–O–Mo bonds to form robust heterostructures. These kinds of heterostructures with strong covalent bonds benefited to boost the charge transfer kinetics of K⁺ and maintained the stability of the structure. In addition, the MXenes-based heterostructures could provide more active sites on the surface for adsorption of K⁺ and offer a 2D diffusion pathway to facilitate the transport of K⁺. The potassium storage capacity was 355 mAh g⁻¹ after 100 cycles (Figure 7b).^[101] Moreover, the pseudocapacitive contribution of MoSe₂/MXene@C heterostructures was as high as 90.2% at the scan rate of 1.2 mV s⁻¹. Cao et al. constructed MXenes and SnS₂ nanosheet heterostructures via a simple hydrothermal reaction.^[102] The vertical SnS₂ nanosheets were uniformly grown on N,S codoped MXene sheets (SnS₂–NSs/MXene). As shown in Figure 7c,d, the morphology and lattice fringes of the SnS₂–NSs/MXene were characterized by scanning electron microscopy (SEM) and high-resolution transmission electron microscopy (HRTEM), which indicated enlarged SnS₂ layer spacing and ensured resulting heterostructure materials with the merits of outstanding electrical conductivity and mechanical stability. Serving as an anode of PIBs, it exhibited excellent cycling performance and rate behavior. The reversible capacity was as high as 206.1 mAh g⁻¹ at a current density of 0.5 A g⁻¹ even after 800 cycles (Figure 7e).^[102] Likewise, the ultrathin SnS₂/Ti₃C₂T_x heterostructures with a thickness of about 5 nm were synthesized by assembling the few-layer SnS₂ and Ti₃C₂T_x.^[103] When used as an anode for PIBs, the ultrathin SnS₂/Ti₃C₂T_x heterostructures demonstrated the remarkable capacity of 462.1 mAh g⁻¹ at 0.1 A g⁻¹ and maintained the reversible capacity of 85.5 mAh g⁻¹ at the high current density of 2.0 A g⁻¹ after 460 cycles. In addition, Zhao et al. designed and synthesized the layer-by-layer heterostructures of PDDA–NPCN/Ti₃C₂ (N-rich porous carbon nanosheets/Ti₃C₂) under the PDDA [poly (diallyl dimethylammonium chloride)], which generated more active sites and enlarged the layer spacing.^[104] As a result, the heterostructures presented outstanding specific capacities (358.4 mAh g⁻¹ after 300 cycles at 100 mA g⁻¹) and great structural stability (252.2 mAh g⁻¹ after 2000 cycles at 1.0 A g⁻¹). Recently, Wu and coworkers obtained the 2D–2D heterostructure

electrode materials of black phosphorene@V₂CT_x (donated as BPE@V₂CT_x), (T = OH or F, x = 2), by an electrostatic attraction assembly without surfactant (Figure 7f).^[60] With 2D interlayer heterostructures, it could make full use of the merits of the expanded interlayer spacing and charge redistribution between adjacent interfaces, which facilitated the K⁺ insertion/extraction and accelerated the K⁺ transport kinetics. They also applied DFT calculations and galvanostatic intermittent titration technique (GITT) to verify the enhanced adsorption of K⁺ and fast diffusion of K⁺ in BPE@V₂CT_x heterostructures. As an anode for PIBs, BPE@V₂CT_x exhibited as high reversible capacity of 593.6 mAh g⁻¹ at 0.1 A g⁻¹ and exceptional cycling stability of 485 mAh g⁻¹ after 3000 cycles at 200 mA g⁻¹, corresponding to 91% capacity retention.^[60] Compared with BPE and V₂CT_x, the BPE@V₂CT_x heterostructures delivered the highest reversible capacity of 570 mAh g⁻¹ under a current density of 0.1 A g⁻¹ after 500 cycles (Figure 7g).

Furthermore, a two-step chemical vapor deposition route was exploited to obtain N-doped graphene/ReSe₂/Ti₃C₂ MXene (3D–2D) heterostructures.^[105] The capacity of N-doped graphene/ReSe₂/Ti₃C₂ MXene reached 395.3 mAh g⁻¹ at 0.1 A g⁻¹. Even at high current densities of 5 and 10 A g⁻¹, it still achieved capacities of 154.7 and 137.5 mAh g⁻¹, respectively. Moreover, DFT calculations revealed the origin of the favored K⁺ adsorption/diffusion and the improved electron conductivity. Compared with bare ReSe₂, G/ReSe₂ possessed a very low bandgap, indicating that G/ReSe₂ brought higher electronic conductivity. These results verified the superiority of the N-doped graphene/ReSe₂/MXene heterostructures.

As emerging 2D nanomaterials, MXenes are usually used as good conductive substrates to support other materials for forming new types of MXenes-based heterostructures. These heterostructures have robust structures achieved by the covalent bonds or vdW interactions, which improve the mechanical properties of the heterostructures and accommodate the huge change of volume. In short, MXenes-based heterostructures show a promising application potential for K storage.

3.3. 2D Transition Metal Dichalcogenides/Transition Metal Oxide-Based Heterostructures

2D TMDs (e.g., MoS₂, MoSe₂, WS₂, WSe₂) classical examples of 2D atomic crystals, and they have been extensively explored for energy storage applications over the past years.^[106–109] In particular, TMDs show huge potential as electrode materials for PIBs, and the K⁺ storage in TMDs is usually via the combination of conversion and insertion reaction, offering higher theoretical specific capacity than carbon-based materials.^[29,109–112] Unfortunately, the low conductivity and brittle structures within the operating voltage restricted the applications of TMDs for K⁺ storage.^[23,29]

Recently, bamboo-like hollow tubes with MoS₂/N-doped C heterostructures were reported as anode materials for PIBs (Figure 8a,b).^[113] The heterostructures stacked by MoS₂ nanosheets and N-doped C layers can effectively enhance the conductivity and protect the structural integrity. Meanwhile, the heterostructures exhibited an expanded interlayer distance up to 1 nm (Figure 8c). DFT results confirmed that the MoS₂/N-doped C atomic interface offered additional active sites to

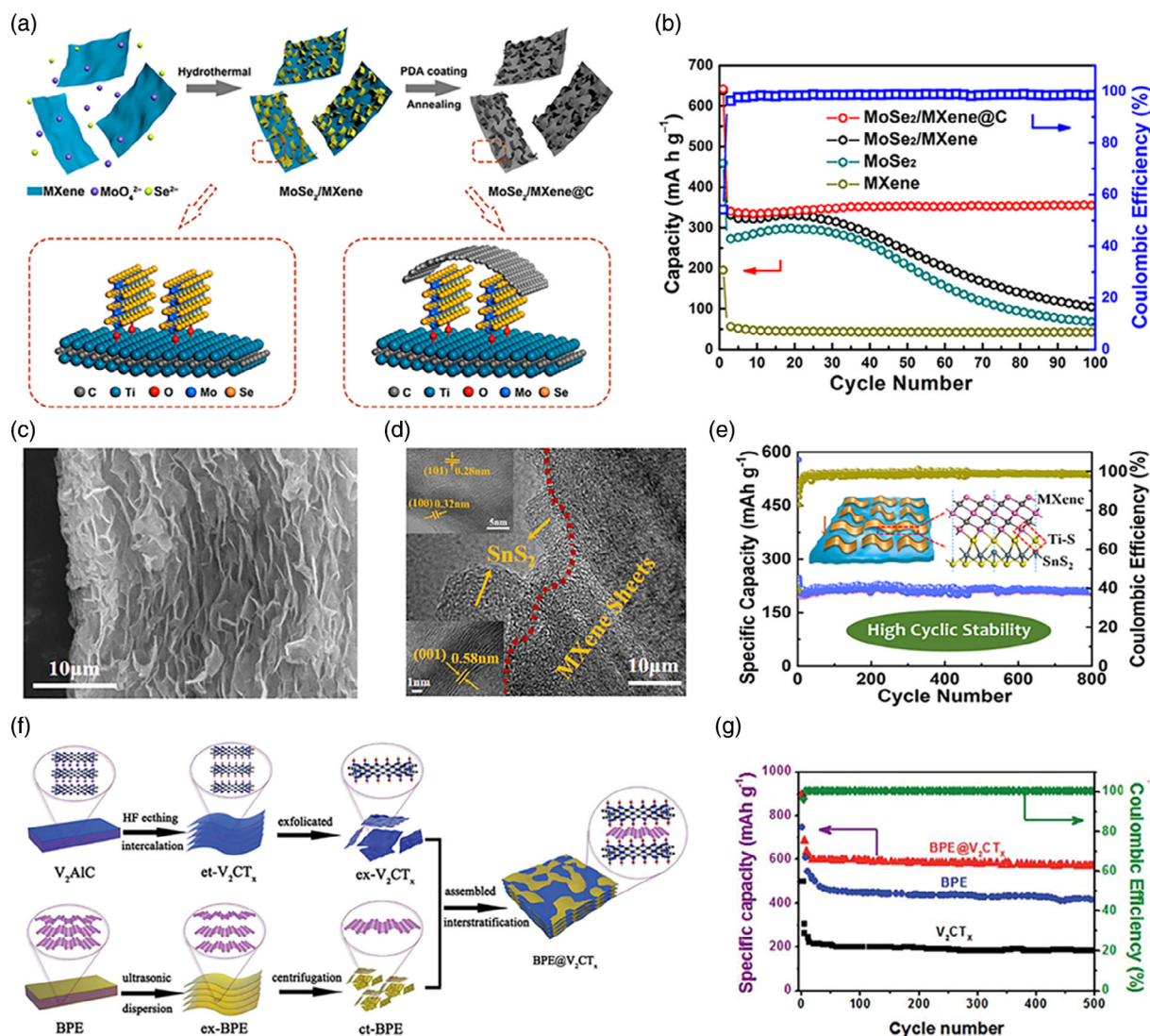


Figure 7. a) Schematic of the preparation of MoSe₂/MXene@C. b) Comparison of cycle performance of MoSe₂/MXene@C, MoSe₂/MXene, MoSe₂, and MXene at 200 mA g⁻¹ along with corresponding CE of MoSe₂/MXene@C. a, b) Reproduced with permission.^[101] Copyright 2019, American Chemical Society. c) SEM and d) HRTEM images of SnS₂-NSs/MXene. e) Long-term cycling performance of SnS₂-NSs/MXene under a current density of 0.5 A g⁻¹. c–e) Reproduced with permission.^[102] Copyright 2021 American Chemical Society. f) Schematic illustration for the preparation of BPE@V₂CT_x heterostructures. g) Cycling stability of BPE, V₂CT_x, and BPE@V₂CT_x as anodes for PIBs at 0.1 A g⁻¹. f, g) Reproduced with permission.^[60] Copyright 2020, Royal Society of Chemistry.

absorb K⁺ and decreased the diffusion energy barrier of K⁺. Therefore, it exhibited long cycling performance of the reversible capacity of 151 mAh g⁻¹ at the current density of 0.5 A g⁻¹ after 1000 cycles.^[113] Zhang et al. fabricated the 2D–2D heterostructures of the dual carbon-coated MoS₂ nanosheets (MoS₂/C@NDG) through a facile hydrothermal method.^[109] These heterostructures not only provided enough space to buffer the volume change and prevent the agglomeration of MoS₂, but also improve the electronic conductivity of MoS₂ and boost the rapid of K⁺ diffusion during cycling. Thus, it delivered a high specific capacity of 443.6 mAh g⁻¹ at 100 mA g⁻¹ and a remarkable rate performance of 176.6 mAh g⁻¹ at 2.0 A g⁻¹.

In addition, multiphase heterostructures were also investigated as PIB electrode materials. For instance, ternary heterostructures of MoS₂-based (denoted as Fe₉S₁₀@MoS₂@C) were designed by introducing Fe₉S₁₀ core for PIBs.^[114] Owing to the different energy bandgap of the Fe₉S₁₀ (0 eV) and MoS₂ (1.17 eV), a strong built-in electric field was formed at the heterointerface, which boosted the fast K⁺ extraction during the charging process. The concentrations of K⁺ on Fe₉S₁₀ and MoS₂ area were different due to the reaction reversibility of Fe₉S₁₀, which helped the fast K⁺ insertion during the discharging process (Figure 8d). The Fe₉S₁₀@MoS₂@C heterostructures demonstrated a high initial capacity of 321 mAh g⁻¹ at 0.2 A g⁻¹ and

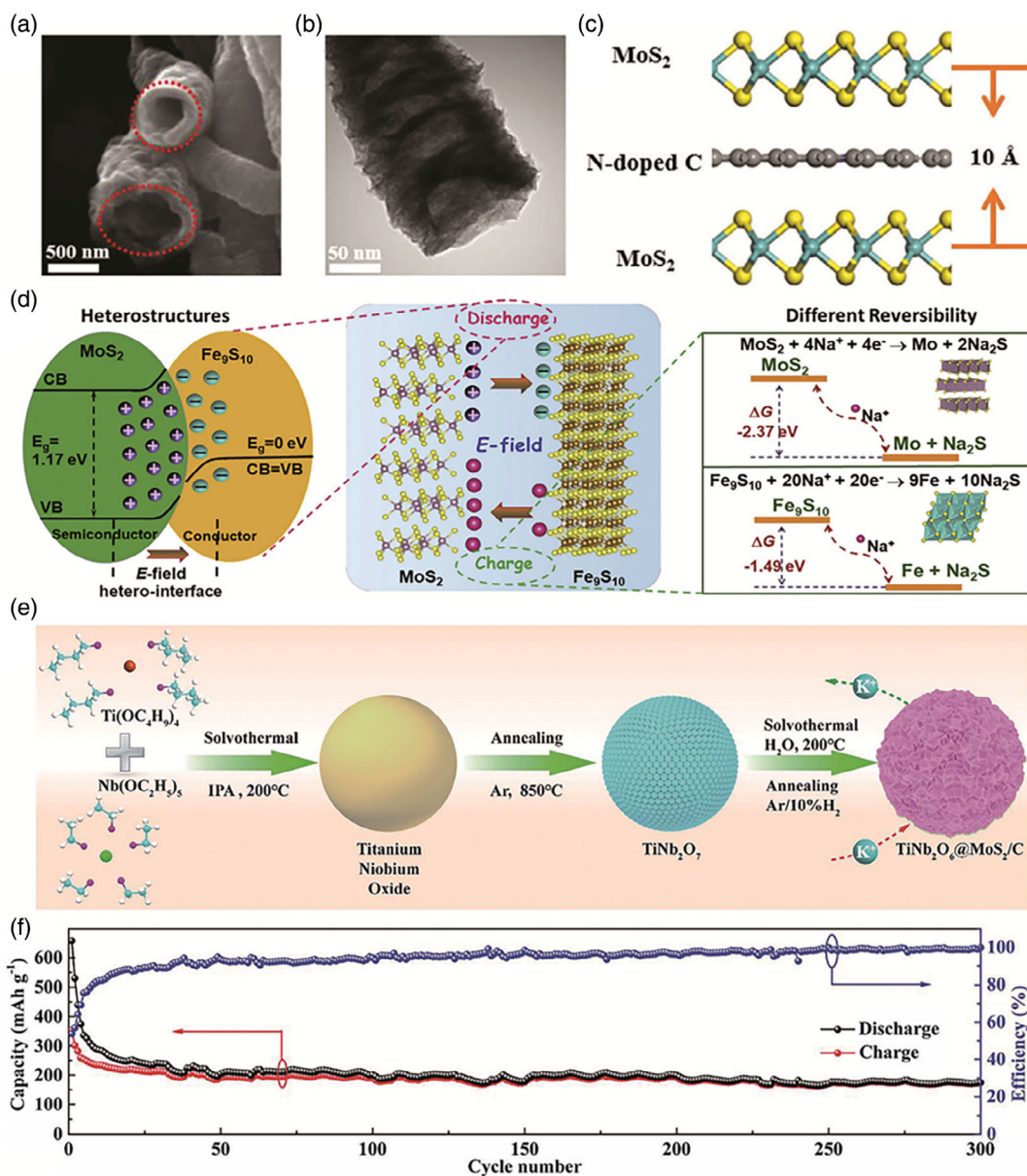


Figure 8. a) SEM image, b) TEM image, and c) crystalline structure of MoS₂/N-doped carbon heterostructures. a–c) Reproduced with permission.^[113] Copyright 2018, Wiley-VCH. d) Schematic illustration of the formation mechanism and direction of internal electric field for Fe₉S₁₀@MoS₂/C during discharge and charge processes. d) Reproduced with permission.^[114] Copyright 2020, Elsevier. e) Schematic illustration of the formation of TiNb₂O₆@MoS₂/C heterostructured microspheres. f) Cycle performance at 1.0 A g⁻¹ of TiNb₂O₆@MoS₂/C heterostructured microspheres. e, f) Reproduced with permission.^[116] Copyright 2019, Royal Society of Chemistry.

good cycling performance (with 95.4% capacity retention) even at a high current density of 2.0 A g⁻¹ after 50 cycles for PIBs.^[114] By combing p-type MoS₂ with n-type Bi₂S₃, carbon-coated Bi₂S₃/MoS₂ heterostructures were synthesized.^[115] The uniform carbon layer could improve the structural stability, and at the same time the carbon-coated Bi₂S₃/MoS₂ heterostructures effectively boosted the charge transport and accelerated the reaction kinetics. Therefore, the enhanced potassium storage performance of carbon-coated Bi₂S₃/MoS₂ heterostructures could be attributed to the synergistic effects of all three components. It maintained

a capacity of 382.8 mAh g⁻¹ at 0.1 A g⁻¹ after 100 cycles. At a high current density of 3 A g⁻¹, the carbon-coated Bi₂S₃/MoS₂ heterostructures still delivered a capacity of 300.2 mAh g⁻¹. Xing et al. also investigated the electrochemical properties of three-layered heterostructure TiNb₂O₆@MoS₂/C core-shell microspheres as an anode for PIBs (Figure 8e).^[116] The core of oxygen-atom-unsaturated metallic TiNb₂O₆ was deemed to be the main reason for enhancing the electron mobility of the microspheres. The porous TiNb₂O₆ core not only could provide more active sites for the tight growth of MoS₂ and restrain the

agglomeration of the MoS₂ nanosheets, but also could availably increase the flexible contact between the heterostructure materials and electrolyte.^[116] As a result, the electrode exhibited outstanding performance with a high capacity of 424 mAh g⁻¹ at 100 mA g⁻¹ after 50 cycles. Even at a high current density of 1.0 A g⁻¹, the average capacity was 175 mAh g⁻¹ after 300 cycles (Figure 8f).^[116] Hierarchical chrysanthemum-like MoS₂/Sb heterostructures were encapsulated into the N-doped graphene.^[117] Benefiting from the advantage of the synergetic effect between the heterointerface of MoS₂ and Sb, the electrode displayed a large specific capacity of 359.5 mAh g⁻¹ at 50 mA g⁻¹. At a current density of 2.0 A g⁻¹, the capacity still reached 233.2 mAh g⁻¹ with a low capacity loss of 0.027% per cycle during 1000 cycles.

1T-MoS₂ has a narrow bandgap and enriched metallic properties, but it is unstable and hard to be directly used for energy storage.^[118–120] Some researchers have prepared 1T-MoS₂-based heterostructures for PIBs. For instance, Wu et al. designed the fewer-layer 1T/2H-MoS₂ nanosheets to be anchored on N-doped carbon nanotube hollow polyhedron (denoted as NCNHP), as shown in Figure 9a.^[121] The heterostructures with the hollow structure created enough voids to alleviate the volume change, resulting in an ultrastable performance of 281.2 mAh g⁻¹ after 500 cycles with a good capacity retention 66.7% (Figure 9b). Moreover, they also assembled full-cell PIBs with 1T/2H-MoS₂/NCNHP as anode and K₂Fe[Fe(CN)₆] as cathode, which presented a lifetime over 100 cycles (136.1 mAh g⁻¹) at 100 mA g⁻¹ (Figure 9c).^[121] Zhou et al. utilized 1T-MoS₂/MoO_x@NC (N-doped carbon) for K⁺ storage.^[122] After 400 cycles, it still had the capacity of 120 mAh g⁻¹ at the current density of 500 mA g⁻¹. The stable electrochemical K⁺ storage property of 1T-MoS₂ was attributed to its good electrical conductivity.

The heterostructures of MoS₂ or MoSe₂ on N-doped carbon (MoS₂/MoSe₂-on-NC) were also fabricated by a sacrificial template and subsequent sulfidation/selenization.^[123] As PIB anode, the MoS₂-on-NC presented a high capacity of 399 mAh g⁻¹ at the current density of 1 A g⁻¹ after 5000 cycles, corresponding to the capacity decay per cycle of 0.0043%. MoSe₂-on-NC also delivered a reversible capacity of 247 mAh g⁻¹ at the current density of 1 A g⁻¹ after 4800 cycles, corresponding to the CE of ≈100%. The unique heterostructures in the composite played two key roles: 1) the built-in electric field effectively accelerates the charge transfer and improves the K⁺ reaction kinetics and 2) the strong covalent bonds (i.e., C—S, C—Se, C—Mo bonds) could maintain structural stability. In addition, Liu et al. also synthesized MoSe₂-MoO₃ quantum dot heterostructures with the help of a sacrificial template.^[28] When used as an anode for PIBs, it displayed the excellent capacity of 308.7 mAh g⁻¹ after 300 cycles at 50 mA g⁻¹. Compared with MoO₃, MoO₂ has a higher conductivity. Thus, Jiang et al. synthesized the heterostructures of MoSe₂@MoO₂ nanostructured materials (Figure 9d).^[124] In the composite, metallic MoO₂ nanoparticles not only improved the electrical conductivity but also prevented ultrathin MoSe₂ nanosheets from being stacked, which resulted in a larger active surface for K⁺ adsorption. The difference in the bandgap between MoSe₂ (1.51 eV) and MoO₂ (0.9 eV) could generate a built-in electric field at the heterointerface, and it thus boosted K⁺ transfer during cycling (Figure 9e). As a result, MoSe₂@MoO₂ was able to deliver a capacity of 255 mAh g⁻¹ at 500 mA g⁻¹ after 100 cycles with a CE close to 100%

(Figure 9f). As for combining with alloy-type materials, the heterostructures of MoSe₂-graphene covalently connected with SnS (SnS@MoSe₂-GR) and were obtained.^[125] It was noted that a built-in electric field was generated at the heterointerface between MoSe₂ and SnS because of the unbalanced charge distribution. It was ensured that the SnS@MoSe₂-GR showed great electrochemical performance. Serving as PIB anode, it maintained a stable capacity of 311.6 at 50 mA g⁻¹ after 100 cycles and 120 mAh g⁻¹ at 500 mA g⁻¹ after 3500 cycles, respectively.

In addition, TMO-based heterostructures were also prepared as electrode materials for PIBs.^[58,126] For example, the hierarchical TiO₂/C tubular heterostructures were synthesized as anodes for PIBs.^[58] DFT calculations and density of state data indicated that the TiO₂/C heterostructures had a lower energy barrier for potassium storage and a higher conductivity than those of TiO₂-C hybrids. Hence, TiO₂/C heterostructures exhibited a reversible capacity of 240.8 mAh g⁻¹ at the current density of 100 mA g⁻¹. Even at 500 mA g⁻¹ after 1200 cycles, the high capacity of 132.8 mAh g⁻¹ could be still maintained.

Compared with the individual 2D TMDs or TMOs, integrating TMDs and/or TMOs-based heterostructures provides more potential for storing K⁺. For example, the heterostructures with various phase components and rich valence states can possess adjustable conductivity properties and tunable bandgaps, which greatly affect the properties of heterostructures materials and thereafter enhanced chemical performance for PIBs. Thus, to enhance the K⁺ storage performance, some factors should be considered in the rational design and regulation of TMDs and/or TMOs-based heterostructures, such as crystal structure, nanosheet size and thickness, and interlayer bonding states.

3.4. Other Heterostructures for PIBs

In recent years, more 2D materials have been exploited.^[127,128] Except for elemental 2D and TMDs/TMOs, the main group of metal chalcogenide 2D materials has also attracted attention, such as SnS and SnS₂.^[129,130] SnS and SnS₂ can generally provide high specific capacities owing to the multielectron reactions and the following alloying reactions.^[46,131,132] In addition, theoretical calculations showed that the diffusion potential of K⁺ at the surface of SnS₂ is very low, so SnS₂ has the potential as a high-density battery material.^[133] However, they could be impeded by the huge volume expansion, which will lead to rapid capacity decay and the unsatisfied lifespan.^[133–135] Thus, developing heterostructure materials with SnS₂ or SnS has been proposed to enhance the cycling performance. Cao et al. constructed layered VS₄/SnS (1D–2D) heterostructures anchored on graphene (VS₄/SnS@C) through solvothermal and sulfidation reaction (Figure 10a).^[136] Owing to the advantage of the heterostructure framework, the composite showed a high specific surface area. At the same time, the different types of SnS and VS₄ could form a built-in electric field at the interface of the heterostructure, which could boost the charge transfer and improve the K⁺ insertion/extraction kinetics. The most important thing is that the presence of S₂²⁻ in the structure could weaken the shuttle effect of polysulfides; thus, the active material VS₄/SnS@C demonstrated better structural stability and electrochemical performance. When being evaluated as an anode for PIBs, VS₄/

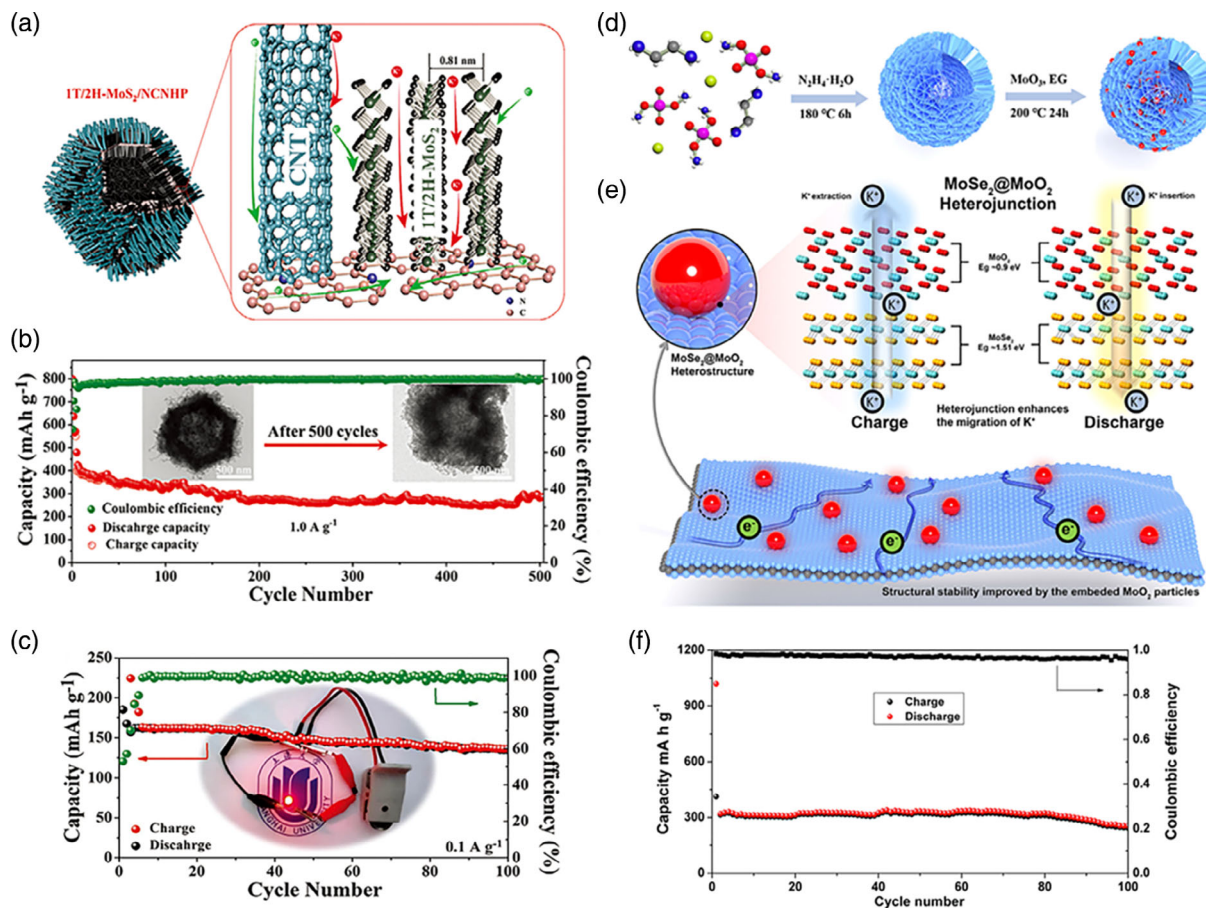


Figure 9. a) Schematic illustration of K⁺ diffusion pathways in 1T/2H-MoS₂/NCNHP heterostructures. b) Cycling performance of 1T/2H-MoS₂/NCNHP at 1.0 A g⁻¹ (insets: the morphology of 1T/2H-MoS₂/NCNHP before and after 500 cycles). c) Cycling performance at 0.1 A g⁻¹ and optical photograph of LED lightened up by K-ion full cell. a–c) Reproduced with permission.^[121] Copyright 2020, Wiley-VCH. d) Schematic illustration of the preparation of MoSe₂@MoO₂ heterostructures. e) Summary of the enhanced ion transportation mechanisms of MoSe₂@MoO₂ heterostructures in PIBs. f) Cycling performance of MoSe₂@MoO₂ heterostructures at 500 mA g⁻¹. d–f) Reproduced with permission.^[124] Copyright 2020, Elsevier.

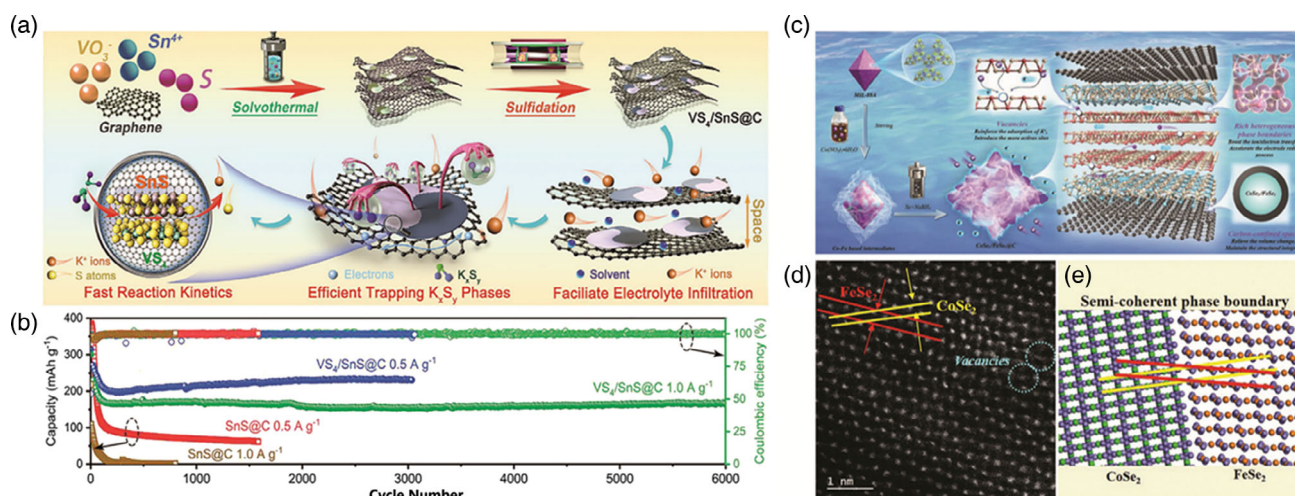


Figure 10. a) Schematic of the fabrication of VS₄/SnS@C heterostructures. b) Ultralong cycling performances of VS₄/SnS@C heterostructures for K⁺ storage. a, b) Reproduced with permission.^[136] Copyright 2021, Wiley-VCH. c) Illustration of fabricating CoSe₂/FeSe₂@C heterostructures. d, e) HAADF-STEM image and the corresponding schematic diagram of the heterostructures of CoSe₂/FeSe₂. c–e) Reproduced with permission.^[141] Copyright 2021, Wiley-VCH.

SnS@C showed a remarkable cycling stability at different current densities, in which a specific capacity of 227 and 168.4 mAh g⁻¹ was retained over 3000 and 6000 cycles at 0.5 and 1 A g⁻¹, respectively (Figure 10b).^[136] Suo et al. synthesized the heterostructures of SnS₂/SnO₂ with good conductive stainless steel mesh (SSM) as a free-standing electrode for PIBs.^[137] Due to the merit of binder-/conductive-additive free and special heterostructures, the SnS₂/SnO₂/SSM electrode produced a reversible specific capacity of 394 mAh g⁻¹ at the current density of 50 mA g⁻¹ over 100 cycles.

Researchers also tried to exploit other heterostructures as PIB electrode materials.^[138] For example, the heterostructures are made up of non-2D materials such as CoSe₂, CoS₂, FeS₂, and FeSe₂.^[139–147] As an example, the hierarchical CoSe₂–FeSe₂@C heterostructures were constructed by applied MOFs as sacrificial template (Figure 10c).^[141] The introduction of FeSe₂ with a narrow bandgap could induce the formation of a built-in electric field inside the material and boost the reaction kinetics of K⁺. More importantly, rich atomic vacancies and a slightly disordered atomic arrangement of CoSe₂–FeSe₂@C heterointerface were certified by high-angle-annular dark-field scanning transmission electron microscopy (HAADF-STEM) (Figure 10d,e), which afforded more active sites during the charging-discharging process. As a result, the heterostructure electrode materials obtained a high capacity of 401.1 mAh g⁻¹ at 0.1 A g⁻¹ and even 275 mAh g⁻¹ at a high current density of 2 A g⁻¹. Suo et al. developed the CoS₂/CuCo₂S₄ hollow sphere heterostructures coated with nitrogen-doped carbon (CoS₂/CuCo₂S₄@NCs).^[142] The CoS₂/CuCo₂S₄@NC electrode maintained a high rate capability of 309 mAh g⁻¹ at 0.5 A g⁻¹ after 250 cycles with ether-based electrolyte. These hollow sphere heterostructures were beneficial for boosting the K⁺ transportation and providing more space for the intercalation/deintercalation of K⁺.

Given the above, constructing heterostructures to change the electronic properties and mitigate the shuttle effect of active materials will guarantee the fast kinetics of K⁺. Moreover, some heterostructures electrode materials with mix-dimension have been successfully fabricated, which are endowed with suitable ion-diffusion channels and a good strain-release property to facilitate ion transport and buffer the severe volume variation during K⁺ insertion/extraction, thus effectively promoting the applications of PIBs.

4. Conclusions and Outlook

In this review, we have presented an overview of the recent progresses on the design, synthesis, and applications of 2D-based heterostructures in particular graphene-, MXenes-, TMDs-, and TMOs-based heterostructures as electrode materials for PIBs. Details in compositions, synthetic methods, and electrochemical properties of these 2D-based heterostructures are summarized in Table 1. As shown in Table 1, the synthesis of 2D-based heterostructures is usually a complex and multistep process that is a combination of different synthetic techniques, including chemical vapor deposition (CVD), hydrothermal, freeze drying, annealing, spray pyrolysis, etching, and so on. Through such a complex and multistep process, different 2D

materials are integrated with other functional materials via either vdW forces or covalent bonds to obtain 2D-based heterostructures. In comparison with individual 2D materials, these 2D-based heterostructures as electrode materials for PIBs exhibit significant improvement in initial CE (ICE), rate performance, and cycling stability, owing to their unique structural, physicochemical, and electronic properties including 1) the enlarged interface contact and vacancies and/or distortions at the heterointerfaces that offer abundant electrochemical active sites for K⁺ storage; 2) the built-in electric field in 2D-based heterostructures that promotes the charge transfer kinetics during the K⁺ insertion/extraction process; and 2) the hierarchical configuration of 2D-based heterostructures which alleviates the volume variation of 2D materials during the charging and discharging process. Although some encouraging advances have been achieved in the past years, much research efforts are needed for pursuing with the aims of developing 2D-based heterostructures for practical PIB applications.

As aforementioned, the K⁺ storage performance of 2D-based heterostructures is highly dependent on their components and morphologies. Even consisting of the same components, changes in morphologies (i.e., the size, shape, and spatial arrangement of each component and/or the ensemble) of 2D-based heterostructures might result in a significant difference in their electrochemical performance. Currently, the synthesis of 2D-based heterostructures is usually a complex and multistep synthesis process, and the experimental conditions in each step have to be well controlled because slight variations in experimental conditions would lead to morphology changes of the as-obtained 2D-based heterostructures and thus influence the electrochemical performance. Therefore, a facile synthetic strategy should be developed to controllably produce 2D-based heterostructures with high consistency in morphologies. Moreover, this synthetic strategy also should be cost effective and scalable, so as to satisfy the industrial-scale production of 2D-based heterostructures for PIBs. Besides the consistency in morphologies, the optimization in components and morphologies of 2D-based heterostructures are also of great significance. The attainable potassium-ion storage capacity of 2D-based heterostructures relates to the theoretical capacity of both host 2D materials and guest functional materials in 2D-based heterostructures. Integrating host 2D materials with one kind of guest functional material that has a high theoretical specific capacity has been demonstrated as an effective way to obtain 2D-based heterostructures with a high specific capacity.^[63,112] However, it should be noted that the overall specific capacity of 2D-based heterostructures will not be the sample sum of the theoretical specific capacity of host 2D materials and guest functional materials. The morphologies of 2D-based heterostructures have to be optimized toward enlarging the interface contact area and hence creating more active sites for K⁺ storage and strengthening the interactions to facilitate K⁺ storage kinetics. Only then will a high specific capacity, which is even higher than the sum of the theoretical specific capacity of host 2D materials and guest functional materials, be achieved and at the same time realize high rate performance. In addition, the K⁺ storage mechanism of 2D-based heterostructures might be different from both host 2D materials and guest functional materials. A better understanding of the effect of the morphologies of 2D-based heterostructures as

Table 1. Summary of the materials, synthetic methods, and electrochemical performance of reported 2D-based heterostructures for PIBs.

Materials	Synthetic methods	Electrode	ICE [%]	Rate performance [mAh g ⁻¹ /mA g ⁻¹]	Cycling stability [mAh g ⁻¹ /mA g ⁻¹ Cycles]	Ref.
SnSb ₂ Te ₄ /G	Multiple ball milling	Anode	77.9	368/100; 153/5000	263.5/500 after 200th	[62]
2D VOPO ₄ -graphene heterostructures	Freeze drying, solution-phase self-assembly	Cathode	–	130/80; 80/3200	135/80 after 1000th 105/160 after 1000th	[48]
Bi ₂ S ₃ @rGO	A visible light-assisted method	Anode	72.7	538/200;	237/2000 after 300th	[83]
rGO@MCSe	Hydrothermal, annealing, freeze drying	Anode	65.3	310.4/500	417.8/500 after 100th	[84]
V ₂ O ₅ nanorod@rGO	Hydrothermal, annealing	Cathode	96	50/2940	271/147 after 50th	[80]
Sb@Sb ₂ O ₃ @N-3DCHs	Spray drying, annealing	Anode	60.5	239/5000	319/2000 after 10000th	[139]
Bi _{0.51} Sb _{0.49} OCl/rGO	Wet chemistry, freeze drying	Anode	55.9	407/100; 319/1000	360/100 after 1000th	[61]
N-doped graphene /ReSe ₂ /Ti ₃ C ₂ MXene	Etching, hydrothermal, Freeze drying	Anode	–	138/10 000	90/5000 after 300th	[105]
MoSe ₂ /MXene@C	Hydrothermal, in situ polymerization, annealing	Anode	54.2	356/200 183/10 000	355/200 after 100th; 243/2000 after 300th	[101]
Ti ₃ C ₂ T _x -MXene NCRib Heterostructures	Etching, hydrothermal	Anode	–	371.1/100; 60.7/5000	201.5/1000 after 1000th	[99]
MXene/MoS ₂ -0.1	Etching, hydrothermal	Anode	66.5	290.7/50; 168.2/500	145.5/200 after 50th	[100]
PDDA-NPCN/Ti ₃ C ₂	Electrostatic attraction self-assembly	Anode	73.2	499.8/100; 191.2/2000	358.4/100 after 300th; 252.2/1000 after 2000th	[104]
BPE@V ₂ CT _x	Ice bath ultrasonic, exfoliated,	Anode	75.1	593.6/100; 306.3/1000,	485/200 after 3000th; 261/2000 after 3000th	[60]
SnS ₂ NSs/MXene	Hydrothermal	Anode	31	342.4/50; 162.6/1000	206.1/500 after 800th	[102]
Cu _{1.75} Se-MXene-CNRib	Hydrothermal, freeze drying, calcinations	Anode	54.9	435.3/100; 161.3/5000	401.3/1 00 after 400th; 305.6/1000 after 400th	[98]
Cu ₁₂ Sb ₄ S ₁₃ /Ti ₃ C ₂ nanosheets	Hydrothermal, freeze drying, sonication	anode	57.2	571.8/50; 188.0/2000	496.7/100 after 200th; 175.6/1000 after 1800th	[97]
SnS ₂ /Ti ₃ C ₂ T _x heterostructures	Wet chemistry	Anode	60.8	462.1/100; 224.7/1000	85.5/2000 after 460th	[103]
MoSe ₂ @MoO ₂ heterojunction	Hydrothermal	Anode	50	365/100; 172/2000	255/500 after 100th	[124]
MoSe ₂ @CNTs	Acid treatment, hydrothermal, annealing	Anode	69.3	209.7/5000; 186.1/10 000	203/2000 after 100th; 159/2000 after 200th	[145]
QDs MoSe ₂ -MoO ₃	Grinding, selenization	Anode	56.3	320.8/50; 148.8/2000	308.7/50 after 300th; 218.5/3000 after 2000th	[28]
MoS ₂ -on-NC MoSe ₂ -on-NC	Sacrificial template, annealing	Anode	–	MoS ₂ -on-NC: 391/500; 130/10 000; MoSe ₂ -on-NC: 328/500; 171/5000	MoS ₂ -on-NC: 399/1000 after 5000th; MoSe ₂ -on-NC: 247/1000 after 4800th	[123]
SnS@MoSe ₂ -GR	Hydrothermal	Anode	73.1	377/100; 106/3000	120/500 after 3500th	[125]
MoS ₂ /N-doped-C	Hydrothermal, annealing	Anode	–	451/50; 131/2000	151/500 after 1000th	[113]
Co ₉ S ₈ /NC@MoS ₂ (DHNCs)	Pyrolysis, Hydrothermal, annealing	Anode	89.1	122/1000	100/1000 after 100th	[144]
1T/2H-MoS ₂ /NCNHP	Hydrothermal, annealing	Anode	63.9	519.2/50	281.2 /1000 after 500th; In the full cell: 136.1/100 after 100th	[136]
TiNb ₂ O ₆ @MoS ₂ /C	Hydrothermal, annealing	Anode	50.45	450/50; 233/1000	424/100 after 50th; 175/1000 after 300th	[116]

Table 1. Continued.

Materials	Synthetic methods	Electrode	ICE [%]	Rate performance [mAh g ⁻¹ /mA g ⁻¹]	Cycling stability [mAh g ⁻¹ /mA g ⁻¹ Cycles]	Ref.
MoS ₂ /C@NDG	Hydrothermal, annealing	Anode	59.3	443.6/100; 176.6/2000	220.7/1000 after 150th	[109]
Bi ₂ S ₃ /MoS ₂ @NC	Hydrothermal	Anode	79.98	300.2/3000	201.6/1000 after 200th	[115]
1T-MoS ₂ /MoO _x @NC	Hydrothermal, annealing	Anode	78.2	257.9/50; 128.8/500	120/500 after 400th; 69.7/800 after 400th	[122]
MoS ₂ /Sb N-doped graphene	Hydrothermal, freeze drying, annealing	Anode	59.3	345.5/50; 235.4/200	296.7/500 after 200th, 170.1/2000 after 1000th	[117]
Fe ₉ S ₁₀ @MoS ₂ @C	In situ polymerization, sulfidation	Anode	71	288/500; 127/5000	389.23/2000 after 50th	[114]
MoS ₂ -WS ₂ -C	Spray pyrolysis, annealing	Anode	65	377/100; 176/5000	350/100 after 100th; 291/1000 after 50th	[112]
Sandwich-like MoS ₂ @SnO ₂ @C	Hydrothermal, annealing	Anode	73	597/50; 345/100;	312/50 after 25th; 250/100 after 20th	[14]
MoS ₂ @rGO	Two-step hydrothermal	Anode	-	679/20; 178/500	381/100 after 100th	[63]
C/MoS ₂ /G	Hydrothermal, annealing	Anode	40	362.5/100; 195.4/10 000	346/500 after 200th; 126.4/5000 after 4000th	[82]
CoSe ₂ -SnSe ₂ @NC	Hydrothermal, annealing	Anode	70	368/100; 249/1000	369/500 after 200th	[147]
SnS ₂ /SnO ₂ /SSM	Hydrothermal	Anode	65.6	470/50; 150/1000	394/50 after 100th; 155/500 after 250th	[137]
CoSe ₂ -FeSe ₂ @C-II	Sacrificial template, annealing	Anode	71.42	420/100; 325/1000	271.4/2000 after 300th	[141]
H-TiO ₂ -C heterostructures	Wet-chemical method	anode	49.1	240.8/100; 114.6/1000	132.8/500 after 1200th	[58]
VS ₄ /SnS@C heterostructures	Hydrothermal, Freeze drying, annealing	Anode	52.2	270.1 /100; 162.1/5000	227/500 after 3000th; 168.4/1000 after 6000th	[136]

well as the interactions between host 2D materials and guest functional materials on the K⁺ storage mechanism of 2D-based heterostructures might lead to optimized synergetic effects for realizing high potassium-ion storage capability. Therefore, theoretical calculations and advanced in/ex situ characterizations should be systematically combined to reveal the potassium-ion storage mechanism of 2D-based heterostructures, providing a guideline for optimizing the morphologies and components of 2D-based heterostructures.

Despite these challenges, the 2D-based heterostructures open a new possibility for breaking the electrochemical property limits of individual 2D materials for K⁺ storage. With further research efforts in this field, it is highly expected that high-performance electrode materials based on stable 2D-based heterostructures will be fabricated to promote the development of PIBs.

Acknowledgements

The authors acknowledge support from the German Research Foundation (DFG: LE 2249/5-1) and the Sino-German Center for Research Promotion (GZ1579). Y.D. would like to acknowledge the China Scholarship Council (no. 201906890026) for financial support.

Open access funding enabled and organized by Projekt DEAL.

Conflict of Interest

The authors declare no conflict of interest.

Keywords

2D-based heterostructures, covalent bonds, electrode materials, potassium-ion batteries, van der Waals forces

Received: December 15, 2021

Revised: January 19, 2022

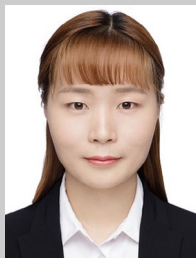
Published online: February 1, 2022

- [1] D. Gielen, F. Boshell, D. Saygin, M. D. Bazilian, N. Wagner, R. Gorini, *Energy Strategy Rev.* **2019**, *24*, 38.
- [2] A. Manthiram, X. Yu, S. Wang, *Nat. Rev. Mater.* **2017**, *2*, 16103.
- [3] Z. Liang, R. Zhao, T. Qiu, R. Zou, Q. Xu, *EnergyChem* **2019**, *1*, 100001.
- [4] K.-B. Wang, Q. Xun, Q. Zhang, *EnergyChem* **2020**, *2*, 100025.
- [5] C. Zhang, H. Zhao, Y. Lei, *Energy Environ. Mater.* **2020**, *3*, 105.
- [6] M. Sha, L. Liu, H. Zhao, Y. Lei, *Energy Environ. Mater.* **2020**, *3*, 56.
- [7] J.-Y. Hwang, S.-T. Myung, Y.-K. Sun, *Adv. Funct. Mater.* **2018**, *28*, 1802938.

- [8] L. Xue, Y. Li, H. Gao, W. Zhou, X. Lü, W. Kaveevitvichai, A. Manthiram, J. B. Goodenough, *J. Am. Chem. Soc.* **2017**, *139*, 2164.
- [9] J. C. Pramudita, D. Sehwat, D. Goonilleke, N. Sharma, *Adv. Energy Mater.* **2017**, *7*, 1602911.
- [10] J. Han, G.-N. Li, F. Liu, M. Wang, Y. Zhang, L. Hu, C. Dai, M. Xu, *Chem. Commun.* **2017**, *53*, 1805.
- [11] L. Li, L. Liu, Z. Hu, Y. Lu, Q. Liu, S. Jin, Q. Zhang, S. Zhao, S.-L. Chou, *Angew. Chem.* **2020**, *132*, 13017.
- [12] Y. Liu, C. Gao, L. Dai, Q. Deng, L. Wang, J. Luo, S. Liu, N. Hu, *Small* **2020**, *16*, 2004096.
- [13] M. Zhou, P. Bai, X. Ji, J. Yang, C. Wang, Y. Xu, *Adv. Mater.* **2021**, *33*, 2003741.
- [14] C. Zhang, Y. Xu, M. Zhou, L. Liang, H. Dong, M. Wu, Y. Yang, Y. Lei, *Adv. Funct. Mater.* **2017**, *27*, 1604307.
- [15] R. Zhang, J. Huang, W. Deng, J. Bao, Y. Pan, S. Huang, C.-F. Sun, *Angew. Chem.* **2019**, *131*, 16626.
- [16] L. Zhang, W. (Alex) Wang, X. Ma, S. Lu, Y. Xiang, *Nano Today* **2021**, *37*, 101074.
- [17] J. Wang, Z. Liu, J. Zhou, K. Han, B. Lu, *ACS Mater. Lett.* **2021**, *3*, 1572.
- [18] S. Zhao, Z. Guo, K. Yan, X. Guo, S. Wan, F. He, B. Sun, G. Wang, *Small Struct.* **2021**, *2*, 2000054.
- [19] X. Kong, Q. Liu, C. Zhang, Z. Peng, Q. Chen, *Chem. Soc. Rev.* **2017**, *46*, 2127.
- [20] F. R. Fan, R. Wang, H. Zhang, W. Wu, *Chem. Soc. Rev.* **2021**, *50*, 10983.
- [21] X. Li, C. Wang, Y. Cao, G. Wang, *Chem. Asian J.* **2018**, *13*, 2742.
- [22] Y. Dong, Z.-S. Wu, S. Zheng, X. Wang, J. Qin, S. Wang, X. Shi, X. Bao, *ACS Nano* **2017**, *11*, 4792.
- [23] Y. Dong, Y. Xu, W. Li, Q. Fu, M. Wu, E. Manske, J. Kröger, Y. Lei, *Small* **2019**, *15*, 1900497.
- [24] Y. Wu, Y. Xu, Y. Li, P. Lyu, J. Wen, C. Zhang, M. Zhou, Y. Fang, H. Zhao, U. Kaiser, Y. Lei, *Nano Res.* **2019**, *12*, 2997.
- [25] X. Zhang, Q. He, X. Xu, T. Xiong, Z. Xiao, J. Meng, X. Wang, L. Wu, J. Chen, L. Mai, *Adv. Energy Mater.* **2020**, *10*, 1904118.
- [26] H. Wang, J. Niu, J. Shi, W. Lv, H. Wang, P. A. van Aken, Z. Zhang, R. Chen, W. Huang, *Small* **2021**, *17*, 2102263.
- [27] K. Yuan, R. Ning, M. Bai, N. Hu, K. Zhang, J. Gu, Q. Li, Y. Huang, C. Shen, K. Xie, *Energy Technol.* **2020**, *8*, 1900796.
- [28] W. Liu, J. Yuan, Y. Hao, H. Maleki Kheimeh Sari, J. Wang, A. Kakimov, W. Xiao, J. Qin, W. Li, C. Xie, J. Hu, J. Peng, X. Li, *J. Mater. Chem. A* **2020**, *8*, 23395.
- [29] C. Zhang, H. Pan, L. Sun, F. Xu, Y. Ouyang, F. Rosei, *Energy Storage Mater.* **2021**, *38*, 354.
- [30] Y. Xu, F. Bahmani, M. Zhou, Y. Li, C. Zhang, F. Liang, S. H. Kazemi, U. Kaiser, G. Meng, Y. Lei, *Nanoscale Horiz.* **2018**, *4*, 202.
- [31] Q. Zhang, X. Cheng, C. Wang, A. M. Rao, B. Lu, *Energy Environ. Sci.* **2021**, *14*, 965.
- [32] X. Ren, Q. Zhao, W. D. McCulloch, Y. Wu, *Nano Res.* **2017**, *10*, 1313.
- [33] J. Li, H. Hu, F. Qin, P. Zhang, L. Zou, H. Wang, K. Zhang, Y. Lai, *Chem. Eur. J.* **2017**, *23*, 14004.
- [34] Y. Wu, C. Zhang, H. Zhao, Y. Lei, *J. Mater. Chem. A* **2021**, *9*, 9506.
- [35] L. Peng, P. Xiong, L. Ma, Y. Yuan, Y. Zhu, D. Chen, X. Luo, J. Lu, K. Amine, G. Yu, *Nat. Commun.* **2017**, *8*, 15139.
- [36] T. Lv, Y. Liu, H. Wang, S. Yang, C. Liu, H. Pang, *Chem. Eng. J.* **2021**, *417*, 128533.
- [37] Y. Wu, Y. Sun, J. Zheng, J. Rong, H. Li, L. Niu, *Chem. Eng. J.* **2021**, *404*, 126565.
- [38] P. Lian, Y. Dong, Z. Wu, S. Zheng, X. Wang, S. Wang, C. Sun, J. Qin, X. Shi, X. Bao, *Nano Energy* **2017**, *40*, 1.
- [39] N. Zheng, G. Jiang, X. Chen, J. Mao, Y. Zhou, Y. Li, *J. Mater. Chem. A* **2019**, *7*, 9305.
- [40] Y. Li, W. Zhong, C. Yang, F. Zheng, Q. Pan, Y. Liu, G. Wang, X. Xiong, M. Liu, *Chem. Eng. J.* **2019**, *358*, 1147.
- [41] H. Huang, R. Xu, Y. Feng, S. Zeng, Y. Jiang, H. Wang, W. Luo, Y. Yu, *Adv. Mater.* **2020**, *32*, 1904320.
- [42] W. Li, D. Wang, Z. Gong, Z. Yin, X. Guo, J. Liu, C. Mao, Z. Zhang, G. Li, *ACS Nano* **2020**, *14*, 16046.
- [43] W. Zhang, J. Ming, W. Zhao, X. Dong, M. N. Hedhili, P. M. F. J. Costa, H. N. Alshareef, *Adv. Funct. Mater.* **2019**, *29*, 1903641.
- [44] X. Liu, T. Ji, H. Guo, H. Wang, J. Li, H. Liu, Z. Shen, *Electrochem. Energy Rev.* **2021**, *139*, 2164.
- [45] Y. Tian, Y. An, H. Wei, C. Wei, Y. Tao, Y. Li, B. Xi, S. Xiong, J. Feng, Y. Qian, *Chem. Mater.* **2020**, *32*, 4054.
- [46] D. Qu, B. Zhao, Z. Song, D. Wang, H. Kong, S. Gan, Y. Ma, X. Dong, D. Han, L. Niu, *J. Mater. Chem. A* **2021**, *9*, 25094.
- [47] P. Du, L. Cao, B. Zhang, C. Wang, Z. Xiao, J. Zhang, D. Wang, X. Ou, *Renewable Sustainable Energy Rev.* **2021**, *151*, 111640.
- [48] J. Cao, L. Wang, D. Li, Z. Yuan, H. Xu, J. Li, R. Chen, V. Shulga, G. Shen, W. Han, *Adv. Mater.* **2021**, *33*, 2101535.
- [49] L. Tao, L. Liu, R. Chang, H. He, P. Zhao, J. Liu, *J. Power Sources* **2020**, *463*, 228172.
- [50] P. Xiao, S. Li, C. Yu, Y. Wang, Y. Xu, *ACS Nano* **2020**, *14*, 10210.
- [51] K. S. Novoselov, A. Mishchenko, A. Carvalho, A. H. Castro Neto, *Science* **2016**, *353*, 6298.
- [52] Y. Liu, Y. Huang, X. Duan, *Nature* **2019**, *567*, 323.
- [53] J. Liu, N. Ma, W. Wu, Q. He, *Chem. Eng. J.* **2020**, *393*, 124719.
- [54] D. Liu, W. Cai, Y. Wang, Y. Zhu, *Appl. Catal. B* **2018**, *236*, 205.
- [55] J. Ren, P. Innocenzi, *Small Struct.* **2021**, *2*, 2100068.
- [56] Q. Yu, Y. Luo, A. Mahmood, B. Liu, H. Cheng, *Electrochem. Energy Rev.* **2019**, *2*, 373.
- [57] D. Zhang, H. Mou, F. Lu, C. Song, D. Wang, *Appl. Catal. B* **2019**, *254*, 471.
- [58] Y. Li, C. Yang, F. Zheng, Q. Pan, Y. Liu, G. Wang, T. Liu, J. Hu, M. Liu, *Nano Energy* **2019**, *59*, 582.
- [59] S. Thurakkal, D. Feldstein, R. Perea-Causin, E. Malic, X. Zhang, *Adv. Mater.* **2021**, *33*, 2005254.
- [60] X. Wu, H. Wang, Z. Zhao, B. Huang, *J. Mater. Chem. A* **2020**, *8*, 12705.
- [61] J. Wang, B. Wang, B. Lu, *Adv. Energy Mater.* **2020**, *10*, 2000884.
- [62] Z. Wu, G. Liang, W. K. Pang, T. Zhou, Z. Cheng, W. Zhang, Y. Liu, B. Johannessen, Z. Guo, *Adv. Mater.* **2020**, *32*, 1905632.
- [63] K. Xie, K. Yuan, X. Li, W. Lu, C. Shen, C. Liang, R. Vajtai, P. Ajayan, B. Wei, *Small* **2017**, *13*, 1701471.
- [64] I. Demiroglu, F. Peeters, O. Gueseren, D. Cakir, C. Sevik, *J. Phys. Chem. Lett.* **2019**, *10*, 727.
- [65] J. Yang, J. Luo, Y. Kuang, Y. He, P. Wen, L. Xiong, X. Wang, Z. Yang, *ACS Appl. Mater. Interfaces* **2021**, *13*, 2072.
- [66] F. Zhang, W. Li, Y. Ma, Y. Tang, X. Dai, *RSC Adv.* **2017**, *7*, 29350.
- [67] C. He, J. Zhang, W. Zhang, T. Li, *J. Phys. Chem. C* **2019**, *123*, 5157.
- [68] G. King'ori, C. Ouma, A. Mishra, G. Amolo, N. Makau, *RSC Adv.* **2020**, *10*, 30127.
- [69] W. Wu, Z. Sun, Q. He, X. Shi, X. Ge, J. Cheng, J. Wang, Z. Zhang, *ACS Appl. Mater. Interfaces* **2021**, *13*, 14752.
- [70] M. Naguib, M. W. Barsoum, Y. Gogotsi, *Adv. Mater.* **2021**, *33*, 2103393.
- [71] X. Wu, Y. Chen, Z. Xing, C. W. K. Lam, S. Pang, W. Zhang, Z. Ju, *Adv. Energy Mater.* **2019**, *9*, 1900343.
- [72] Y. Jiang, F. Guo, Y. Liu, Z. Xu, C. Gao, *SusMat* **2021**, *1*, 304.
- [73] Z. Ju, P. Li, G. Ma, Z. Xing, Q. Zhuang, Y. Qian, *Energy Storage Mater.* **2018**, *11*, 38.
- [74] L. Ma, Y. Lv, J. Wu, C. Xia, Q. Kang, Y. Zhang, H. Liang, Z. Jin, *Nano Res.* **2021**, *14*, 4442.
- [75] K. Share, A. Cohn, R. Carter, B. Rogers, C. Pint, *ACS Nano* **2016**, *10*, 9738.
- [76] X. Ge, S. Liu, M. Qiao, Y. Du, Y. Li, J. Bao, X. Zhou, *Angew. Chem. Int. Ed.* **2019**, *58*, 14578.

- [77] L. Fang, J. Xu, S. Sun, B. Lin, Q. Guo, D. Luo, H. Xia, *Small* **2019**, *15*, 1804806.
- [78] X. Cheng, D. Li, Y. Wu, R. Xu, Y. Yu, *J. Mater. Chem. A* **2019**, *7*, 4913.
- [79] H. Wang, L. Wang, L. Wang, Z. Xing, X. Wu, W. Zhao, X. Qi, Z. Ju, Q. Zhuang, *Chem. Eur. J.* **2018**, *24*, 13897.
- [80] P. Vishnuprakash, C. Nithya, M. Premalatha, *Electrochim Acta* **2019**, *309*, 234.
- [81] P. Xiong, F. Zhang, X. Zhang, S. Wang, H. Liu, B. Sun, J. Zhang, Y. Sun, R. Ma, Y. Bando, C. Zhou, Z. Liu, T. Sasaki, G. Wang, *Nat. Commun.* **2020**, *11*, 3297.
- [82] B. Luo, P. Wu, J. Zhang, L. Cao, C. Wang, B. Lu, B. Zhang, X. Ou, *Nano Res.* **2021**, *14*, 3854.
- [83] Y. Liu, M. Li, Y. Zheng, H. Lin, Z. Wang, W. Xin, C. Wang, F. Du, *Nanoscale* **2020**, *12*, 24394.
- [84] Z. Sun, X. Wu, J. Xu, D. Qu, B. Zhao, Z. Gu, W. Li, H. Liang, L. Gao, Y. Fan, K. Zhou, D. Han, S. Gan, Y. Zhang, L. Niu, *Small* **2020**, *16*, 1907670.
- [85] Y. Gogotsi, Q. Huang, *ACS Nano* **2021**, *15*, 5775.
- [86] J. Yang, Z. Pan, J. Zhong, S. Li, J. Wang, P.-Y. Chen, *Energy Storage Mater.* **2021**, *36*, 257.
- [87] Y. Bai, C. Liu, T. Chen, W. Li, S. Zheng, Y. Pi, Y. Luo, H. Pang, *Angew. Chem. Int. Ed.* **2021**, *60*, 25318.
- [88] A. Rafieerad, A. Amiri, G. L. Sequiera, W. Yan, Y. Chen, A. A. Polycarpou, S. Dhingra, *Adv. Funct. Mater.* **2021**, *31*, 2100015.
- [89] F. Ming, H. Liang, W. Zhang, J. Ming, Y. Lei, A. Emwas, H. N. Alshareef, *Nano Energy* **2019**, *62*, 853.
- [90] Z. Li, Y. Wu, *Small* **2019**, *15*, 1804736.
- [91] J. Yan, C. E. Ren, K. Maleski, C. B. Hatter, B. Anasori, P. Urbankowski, A. Sarycheva, Y. Gogotsi, *Adv. Funct. Mater.* **2017**, *27*, 1701264.
- [92] P. Zhang, D. Wang, Q. Zhu, N. Sun, F. Fu, B. Xu, *Nano-Micro Lett.* **2019**, *11*, 81.
- [93] M. R. Lukatskaya, O. Mashtalir, C. E. Ren, Y. Dall'Agnese, P. Rozier, P. L. Taberna, M. Naguib, P. Simon, M. W. Barsoum, Y. Gogotsi, *Science* **2013**, *341*, 1502.
- [94] J. Mei, T. Liao, Z. Sun, *Energy Environ. Mater.* **2021**, *5*, 115.
- [95] C. Chen, X. Xie, B. Anasori, A. Sarycheva, T. Makaryan, M. Zhao, P. Urbankowski, L. Miao, J. Jjiang, Y. Gogotsi, *Angew. Chem. Int. Ed.* **2018**, *57*, 1846.
- [96] R. Zhao, Z. Qian, Z. Liu, D. Zhao, X. Hui, G. Jiang, C. Wang, L. Yin, *Nano Energy* **2019**, *65*, 104037.
- [97] Y. Cao, Y. Zhang, H. Chen, S. Qin, L. Zhang, S. Guo, H. Yang, *Adv. Funct. Mater.* **2021**, *2*, 2108574.
- [98] J. Cao, Z. Sun, J. Li, Y. Zhu, Z. Yuan, Y. Zhang, D. Li, L. Wang, W. Han, *ACS Nano* **2021**, *15*, 3423.
- [99] J. Cao, J. Li, D. Li, Z. Yuan, Y. Zhang, V. Shulga, Z. Sun, W. Han, *Nano-Micro Lett.* **2021**, *13*, 113.
- [100] J. Li, B. Rui, W. Wei, P. Nie, L. Chang, Z. Le, M. Liu, H. Wang, L. Wang, X. Zhang, *J Power Sources* **2020**, *449*, 227481.
- [101] H. Huang, J. Cui, G. Liu, R. Bi, L. Zhang, *ACS Nano* **2019**, *13*, 3448.
- [102] Y. Cao, H. Chen, Y. Shen, M. Chen, Y. Zhang, L. Zhang, Q. Wang, S. Guo, H. Yang, *ACS Appl. Mater. Interfaces* **2021**, *13*, 17668.
- [103] H. Liu, Y. He, H. Zhang, S. Wang, K. Cao, Y. Jjiang, X. Liu, Q. Jing, *J. Colloid Interface Sci.* **2022**, *606*, 167.
- [104] R. Zhao, H. Di, X. Hui, D. Zhao, R. Wang, C. Wang, L. Yin, *Energy Environ. Sci.* **2020**, *13*, 246.
- [105] Z. Xia, X. Chen, H. Ci, Z. Fan, Y. Yi, W. Yin, N. Wei, J. Cai, Y. Zhang, J. Sun, *J. Energy Chem.* **2021**, *53*, 155.
- [106] H. Dong, Y. Xu, C. Zhang, Y. Wu, M. Zhou, L. Liu, Y. Dong, Q. Fu, M. Wu, Y. Lei, *Inorg. Chem. Front.* **2018**, *5*, 3099.
- [107] X. Zhang, Y. Xiong, L. Zhang, Z. Hou, Y. Qian, B. Johannessen, Y. Tang, J. Luo, H. Wang, Z. Guo, *Inorg. Chem. Front.* **2021**, *8*, 1271.
- [108] S. Chong, X. Wei, Y. Wu, L. Sun, C. Shu, Q. Lu, Y. Hu, G. Cao, W. Huang, *ACS Appl. Mater. Interfaces* **2021**, *13*, 13158.
- [109] J. Zhang, P. Cui, Y. Gu, D. Wu, S. Tao, B. Qian, W. Chu, L. Song, *Adv. Mater. Interfaces* **2019**, *6*, 1901066.
- [110] J. Zhou, L. Wang, M. Yang, J. Wu, F. Chen, W. Huang, N. Han, H. Ye, F. Zhao, Y. Li, Y. Li, *Adv. Mater.* **2017**, *29*, 1702061.
- [111] S. Chen, D. Zhao, L. Chen, G. Liu, Y. Ding, Y. Cao, Z. Chen, *Small Struct.* **2021**, *2*, 2100082.
- [112] J. H. Choi, G. D. Park, Y. C. Kang, *Chem. Eng. J.* **2021**, *408*, 127278.
- [113] B. Jia, Q. Yu, Y. Zhao, M. Qin, W. Wang, Z. Liu, C. Lao, Y. Liu, H. Wu, Z. Zhang, X. Qu, *Adv. Funct. Mater.* **2018**, *28*, 1803409.
- [114] C. Zhang, F. Han, F. Wang, Q. Liu, D. Zhou, F. Zhang, S. Xu, C. Fan, X. Li, J. Liu, *Energy Storage Mater.* **2020**, *24*, 208.
- [115] Y. Qin, Y. Zhang, J. Wang, J. Zhang, Y. Zhai, H. Wang, D. Li, *ACS Appl. Mater. Interfaces* **2020**, *12*, 42902.
- [116] L. Xing, Q. Yu, B. Jiang, J. Chu, C. Lao, M. Wang, K. Han, Z. Liu, Y. Bao, W. Wang, *J. Mater. Chem. A* **2019**, *7*, 5760.
- [117] L. Cao, B. Zhang, H. Xia, C. Wang, B. Luo, X. Fan, J. Zhang, X. Ou, *Chem. Eng. J.* **2020**, *387*, 124060.
- [118] X. Geng, Y. Jiao, Y. Han, A. Mukhopadhyay, L. Yang, H. Zhu, *Adv. Funct. Mater.* **2017**, *27*, 1702998.
- [119] S. Venkateshwaran, T. Partheeban, M. Sasidharan, S. M. Senthil Kumar, *Energy Fuels* **2021**, *35*, 2683.
- [120] J. Bai, B. Zhao, J. Zhou, J. Si, Z. Fang, K. Li, H. Ma, J. Dai, X. Zhu, Y. Sun, *Small* **2019**, *15*, 1805420.
- [121] K. Wu, X. Cao, M. Li, B. Lei, J. Zhan, M. Wu, *Small* **2020**, *16*, 2004178.
- [122] Y. Zhou, M. Zhang, Q. Han, Y. Liu, Y. Wang, X. Sun, X. Zhang, C. Dong, F. Jiang, *Chem. Eng. J.* **2022**, *428*, 131113.
- [123] M. Ma, S. Zhang, Y. Yao, H. Wang, H. Huang, R. Xu, J. Wang, X. Zhou, W. Yang, Z. Peng, X. Wu, Y. Hou, Y. Yu, *Adv. Mater.* **2020**, *32*, 2000958.
- [124] Q. Jiang, S. Hu, L. Wang, Z. Huang, H. Yang, X. Han, Y. Li, C. Lv, Y. He, T. Zhou, J. Hu, *Appl. Surf. Sci.* **2020**, *505*, 144573.
- [125] X. Wang, S. Zhang, Y. Shan, L. Chen, G. Gao, X. Zhu, B. Cao, X. He, *Energy Storage Mater.* **2021**, *37*, 55.
- [126] Z. Wang, X. Yan, F. Wang, T. Xiong, M. Balogun, H. Zhou, J. Deng, *Carbon* **2021**, *174*, 556.
- [127] S. Zheng, Y. Sun, H. Xue, P. Braunstein, W. Huang, H. Pang, *Natl. Sci. Rev.* **2021**, <https://doi.org/10.1093/nsr/nwab197>.
- [128] W. Li, X. Guo, P. Geng, M. Du, Q. Jing, X. Chen, G. Zhang, H. Li, Q. Xu, P. Braunstein, H. Pang, *Adv. Mater.* **2021**, *33*, 2105163.
- [129] L. Wu, H. Shao, C. Yang, X. Feng, L. Han, Y. Zhou, W. Du, X. Sun, Z. Xu, X. Zhang, F. Jiang, C. Dong, *Nanomaterials* **2021**, *11*, 1932.
- [130] D. Bin, S. Duan, X. Lin, L. Liu, Y. Liu, Y. Xu, Y. Sun, X. Tao, A. Cao, L. Wan, *Nano Energy* **2019**, *60*, 912.
- [131] K. Cao, S. Wang, Y. Jia, D. Xu, H. Liu, K. Huang, Q. Jing, L. Jiao, *Chem. Eng. J.* **2021**, *406*, 126902.
- [132] J. Rehman, X. Fan, W. T. Zheng, *Appl. Surf. Sci.* **2019**, *496*, 143625.
- [133] D. Li, L. Dai, X. Ren, F. Ji, Q. Sun, Y. Zhang, L. Ci, *Energy Environ. Sci.* **2021**, *14*, 424.
- [134] Y. Lu, A. P. V. K. Saroja, R. Wei, Y. Xu, *Cell Rep. Phys. Sci.* **2021**, *2*, 100555.
- [135] K. Chen, S. Chong, L. Yuan, Y. Yang, H. Tuan, *Energy Storage Mater.* **2021**, *39*, 239.
- [136] L. Cao, B. Luo, B. Xu, J. Zhang, C. Wang, Z. Xiao, S. Li, Y. Li, B. Zhang, G. Zou, H. Hou, X. Ou, X. Ji, *Adv. Funct. Mater.* **2021**, *31*, 2103802.
- [137] G. Suo, D. Li, L. Feng, X. Hou, X. Ye, L. Zhang, Q. Yu, Y. Yang, W. Wang, *J. Mater. Sci. Technol.* **2020**, *55*, 167.
- [138] F. Wu, M. Liu, Y. Li, X. Feng, K. Zhang, Y. Bai, X. Wang, C. Wu, *Electrochem. Energy Rev.* **2021**, *4*, 382.

- [139] B. Chen, L. Yang, X. Bai, Q. Wu, M. Liang, Y. Wang, N. Zhao, C. Shi, B. Zhou, C. He, *Small* **2021**, *17*, 2006824.
- [140] H. Wu, S. Lu, S. Xu, J. Zhao, Y. Wang, C. Huang, A. Abdelkader, W. A. Wang, K. Xi, Y. Guo, S. Ding, G. Gao, R. V. Kumar, *ACS Nano* **2021**, *15*, 2506.
- [141] H. Shan, J. Qin, Y. Ding, H. M. K. Sari, X. Song, W. Liu, Y. Hao, J. Wang, C. Xie, J. Zhang, X. Li, *Adv. Mater.* **2021**, *33*, 2102471.
- [142] G. Suo, S. Musab Ahmed, Y. Cheng, J. Zhang, Z. Li, X. Hou, Y. Yang, X. Ye, L. Feng, L. Zhang, Q. Yu, *J. Colloid Interface Sci.* **2021**, *608*, 275.
- [143] C. Dong, L. Wu, Y. He, Y. Zhou, X. Sun, W. Du, X. Sun, L. Xu, F. Jiang, *Small* **2020**, *16*, 2004580.
- [144] Y. Han, W. Li, K. Zhou, X. Wu, H. Wu, X. Wu, Q. Shi, G. Diao, M. Chen, *ChemNanoMat* **2020**, *6*, 132.
- [145] Y. Wu, Q. Zhang, Y. Xu, R. Xu, L. Li, Y. Li, C. Zhang, H. Zhao, S. Wang, U. Kaiser, Y. Lei, *ACS Appl. Mater. Interfaces* **2021**, *13*, 18838.
- [146] Z. Chen, D. Yin, M. Zhang, *Small* **2018**, *14*, 1703818.
- [147] D. Yeol Jo, S. Park, *Appl. Surf. Sci.* **2021**, *571*, 151293.



Yulian Dong received her master's degree in the School of Environmental and Chemical Engineering, Shanghai University, in 2019. She is currently being sponsored by China Scholarship Council (CSC) as a Ph.D. candidate at Technology University of Ilmenau under the supervision of Professor Yong Lei. Her research interest focuses on functional nanostructures for sodium- and potassium-ion batteries.



Chengzhan Yan received his M.S. in chemistry from Wenzhou University in 2020. He is currently a Ph.D. student under the supervision of Professor Yong Lei at the Technical University of Ilmenau in Germany. His research interests focus on the construction and functionalization of nanomaterials for energy storage and conversion.



Huaping Zhao obtained his Ph.D. in materials science from the State Key Laboratory of Crystal Materials of Shandong University in 2007. Following two years of postdoctoral research at the Institute of Chemistry (Chinese Academy of Sciences, 2007–2009), he was employed as a scientist by the University of Muenster from 2009 to 2011. Since 2012, he has been a senior scientist (permanent) in Professor Yong Lei's group at the Technical University of Ilmenau, Germany. His current research focus is the design and fabrication of functional nanostructures for energy storage and conversion.



Yong Lei is professor and head of Group (Chair) of Applied Nano-Physics at Technical University of Ilmenau, Germany. He began working in Germany in 2003 as an Alexander von Humboldt fellow at the Karlsruhe Institute of Technology. Since 2006, he has been a group leader at the University of Muenster and a junior professor. In 2011, he joined the Technical University of Ilmenau as a professor. His research focus is on template-based nanostructuring, energy conversion and storage devices, and optoelectronic applications of functional nanostructures. He has received prestigious European and German funding awards, such as two European Research Council Grants.